REVIEW

All-Solid-State Z-Scheme Photocatalytic Systems

Peng Zhou, Jiaguo Yu, and Mietek Jaroniec**

The current rapid industrial development causes the serious energy and environmental crises. Photocatalyts provide a potential strategy to solve these problems because these materials not only can directly convert solar energy into usable or storable energy resources but also can decompose organic pollutants under solar-light irradiation. However, the aforementioned applications require photocatalysts with a wide absorption range, long-term stability, high charge-separation efficiency and strong redox ability. Unfortunately, it is often difficult for a single-component photocatalyst to simultaneously fulfill all these requirements. The artificial heterogeneous Z-scheme photocatalytic systems, mimicking the natural photosynthesis process, overcome the drawbacks of single-component photocatalysts and satisfy those aforementioned requirements. Such multi-task systems have been extensively investigated in the past decade. Especially, the all-solid-state Z-scheme photocatalytic systems without redox pair have been widely used in the water splitting, solar cells, degradation of pollutants and CO_2 conversion, which have a huge potential to solve the current energy and environmental crises facing the modern industrial development. Thus, this review gives a concise overview of the all-solid-state Z-scheme photocatalytic systems, including their composition, construction, optimization and applications.

1. Introduction

Coal and oil, two most important fossil fuels in the modern industrial development, have been over-exploited in the past decades. Due to their limited reserves and non-renewability, coal and oil cannot satisfy the requirement for continuous industrial growth. Though some advancements have been made in the development of new renewable and realistic sources such as hydroelectric power and wind power, the geographical and ecological factors seriously impede their further applications. Besides the energy-related problems, there are serious environmental concerns associated with industrial activities that face the modern society. Hence, an effective solution is necessary to solve the current energy and environmental crises facing the modern industrial development. Photocatalysis is a light-driven chemical process over the surface of a photocatalyst that can produce hydrogen from water (see **Figure 1**a),[1–3] convert solar energy into electric energy (see Figure 1b),[4,5] degrade organic pollutants (see Figure 1c)[6–8] and reduce CO_2 into organic fuels (see Figure 1d).[9–11] Considering the sustainability of solar energy, photocatalysis has a huge potential to solve the aforementioned crises. However, in practical applications, the performance of photocatalysts is greatly limited by two conditions: (a) the energy ($h\nu$) of available photon should be larger than the energy gap (E_g) of photocatalyst; (b) the redox potential of reactants should be located between the bottom of the conduction band (BCB) and the top of the valence band (TVB) of the photocatalyst. The former suggests that a narrow band gap can promote the efficient utilization of solar light. In contrast, the latter implies that a more negative BCB potential and a more positive TVB potential are thermodynamically beneficial for the reduction and oxidation of reactants, respectively. This will broaden the band gap of a photocatalyst, leading to the poor solar-light absorption. It is clear that the two conditions above are mutually exclusive. Therefore, it is difficult for the single-component photocatalyst to simultaneously possess wide light-absorption range and strong redox ability. Moreover, in the single-component photocatalysts, the photogenerated electrons in the CB easily return to the VB and recombine with the photogenerated holes, which seriously reduces the utilization efficiency of solar energy.[12,13] This can be overcome by designing proper heterogeneous photocatalytic systems. As shown in a heterojunction-type photocatalytic system (**Figure 2**), the photogenerated electrons in the CB of the photocatalyst I (PC I) migrate to the CB of the photocatalyst II (PC II), while the photogenerated holes in the VB of PC II move to the VB of PC I.[14–19] As a result, the photogenerated electrons and holes are spatially isolated, which greatly inhibits their undesirable recombination. However, the disadvantage is that the redox ability of photogenerated electrons and holes is weakened after charge transfer because the TVB potential of PC I is less positive than that of PC II and the BCB potential of PC II is less negative than that of PC I. Hence, it is difficult for the present heterojunction-type photocatalytic system to simultaneously possess the high charge-separation efficiency and strong redox ability. Thus, it is necessary to explore a new-type photocatalytic system to solve the aforementioned problems.

P. Zhou, Prof. J. G. Yu
State Key Laboratory of Advanced Technology for Materials Synthesis and Processing
Wuhan University of Technology
Wuhan 430070, P.R. China
E-mail: jiaguoyu@yahoo.com
Prof. M. Jaroniec
Department of Chemistry and Biochemistry
Kent State University
Kent, Ohio 44242, USA
E-mail: jaroniec@kent.edu

DOI: 10.1002/adma.201400288

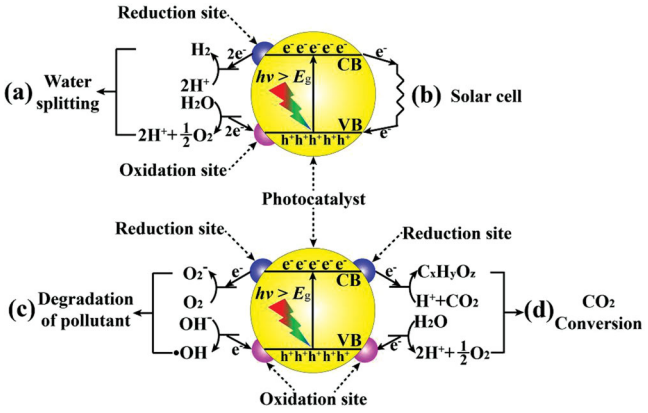

Figure 1. Photocatalytic mechanisms of water splitting, solar cell, degradation of pollutants, CO_2 reduction via one-step photoexcitation. CB and VB represent the conduction and valence bands, respectively.

In nature, photosynthesis that converts H_2O and CO_2 into carbohydrate and O_2 in plants, resembles the so-called Z-scheme photocatalytic process, which involves a two-step photoexcitation (see **Figure 3**).[20,21] First, the electrons in the highest occupied molecular orbital (HOMO) of an oxygen-evolving complex labeled as photosystem II (PS II) are excited to its lowest unoccupied molecular orbital (LUMO) under solar light. Then, the photogenerated electrons in LUMO of PS II are transferred to HOMO of ferredoxin-NAPD reductase labeled as photosystem I (PS I) through the electron mediator. Further, the electrons in HOMO of PS I are excited to its LUMO. As a result, the photogenerated electrons and holes are left in the LUMO of PS I and the HOMO of PS II, respectively. This process is different from the heterojunction-type charge transfer mechanism mentioned above. Finally, the photogenerated electrons in the LUMO of PS I are used to reduce CO_2, while the photogenerated holes in the HOMO of PS II are used to oxidize H_2O. Thus, the Z-scheme photocatalytic system shows the strong reducibility of PS I and the strong oxidizability of

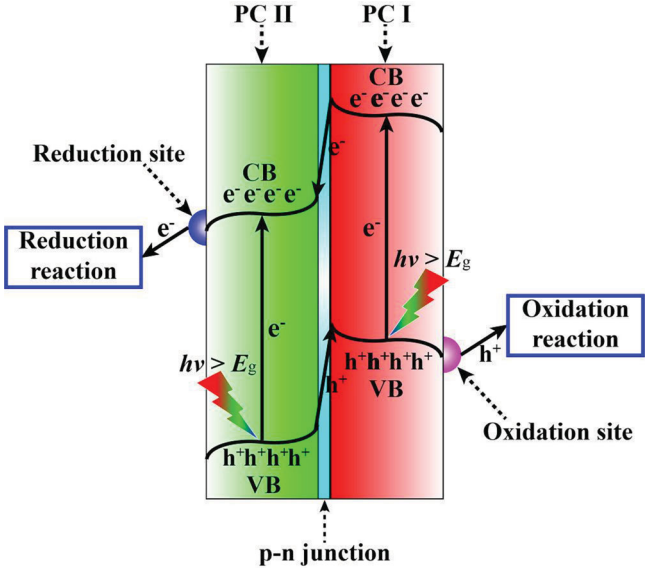

Figure 2. Charge transfer in a heterojunction-type photocatalytic system.

Peng Zhou obtained his B.S degree from Wuhan University of Technology, China, in 2011. From 2011 to present, he works in Prof. Yu's group as a master. His current research concentrates on the synthesis and properties of nanostructured Z-scheme photocatalytic materials.

Jiaguo Yu received his BS and MS in chemistry from Huazhong Normal University and Xi'an Jiaotong University, respectively; his PhD in Materials Science in 2000 from Wuhan University of Technology. In 2000, he became a Professor at Wuhan University of Technology. His current research interests include semiconductor photocatalysis, photocatalytic hydrogen production, CO_2 reduction to hydrocarbon fuels, dye-sensitized solar cells and so on. More information can be found on: http://www.researcherid.com/rid/G-4317–2010.

Mietek Jaroniec received his MS and PhD from M. Curie-Sklodowska University (Poland) in 1972 and 1976; afterward, he was appointed as a faculty at the same University. Since 1991, he is Professor of Chemistry at Kent State University, Kent, Ohio (USA). His research interests include interfacial chemistry and chemistry of materials, especially adsorption at the gas/solid and liquid/solid interfaces and nanoporous materials. At Kent State he has established a vigorous research program in the area of nanomaterials such as ordered mesoporous silicas, organosilicas, inorganic oxides, carbon nanostructures, and nanostructured catalysts/photocatalysts, focusing on their synthesis, characterization and environmental and energy-related applications.

PS II. Therefore, it is likely that an excellent redox ability can be achieved in the Z-scheme photocatalytic system obtained by combining two narrow-bandgap semiconductors, which is beneficial for enhancing absorption of visible light. Considering

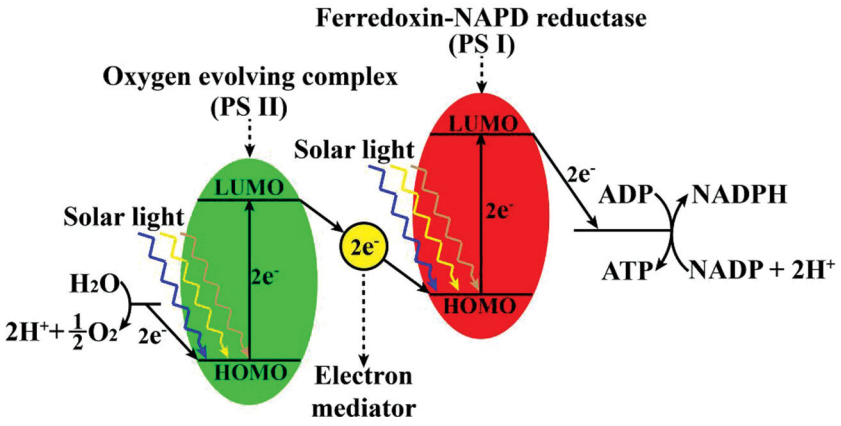

Figure 3. Z-scheme photocatalytic mechanism in natural photosynthesis system.

these unique advantages of the natural Z-scheme photocatalytic system, the artificial Z-scheme photocatalytic systems have been widely investigated in the past three decades, resulting in tremendous developments in this exciting area of research.

Similar to the heterojunction-type photocatalytic system, the artificial Z-scheme photocatalytic system also features the spatial isolation of photogenerated electrons and holes, which reduces the bulk electron-hole recombination. Moreover, the aggregation of photogenerated electrons in the CB of PS I makes PS I an electron-rich region, which can suppress the photo-oxidation of PS I. Similarly, the aggregation of photogenerated holes in the VB of PS II makes PS II a rich-hole region, which can protect PS II from the photo-reduction. However, this also reveals that PS II and PS I can easily suffer from the photo-oxidation and photo-reduction, respectively. Hence, a photocatalyst with weak resistance to photo-oxidation cannot be used as PS II. In the same way, a photocatalyst with weak resistance to photo-reduction is not suitable as PS I. Moreover, the number of photogenerated electrons and holes in the Z-scheme photocatalytic system is just half of that in the heterojunction-type photocatalytic system under same conditions because of the electron-hole recombination in the former. Even then, the Z-scheme photocatalytic systems still receive a lot of attention due to the unique electron transfer.

In the artificial Z-scheme photocatalytic systems, the electron acceptor/donor (A/D) pair is a common electron mediator.[22,23] As shown in **Figure 4**, the Z-scheme photocatalytic system, labeled as PS-A/D-PS, consists of A/D pair, PS II and PS I. No physical contact exists between PS II and PS I. The electron transfer from the CB of PS II to the VB of PS I is fully dependent on the following redox reactions of A/D pair:

$$A + e^- \rightarrow D(\text{CB of PS II}) \quad (1)$$

$$D + h^+ \rightarrow A(\text{VB of PS I}) \quad (2)$$

Firstly, the electron acceptor is reduced into the electron donor after absorbing a photogenerated electron from the CB of PS II. Then the produced electron donor is oxidized into the electron acceptor by the photogenerated hole from the VB of PS I. Thus, with the support of A/D pair, the photogenerated electron is indirectly transferred from the CB of PS II to the VB of PS I. Finally, the photogenerated electron in the CB of PS I and the photogenerated hole in the VB of PS II participates the reduction and oxidation processes with reactants, respectively. It should be noted that the electron acceptor and donor can also react with the photogenerated electron in the CB of PS I (3) and hole in the VB of PS II (4), respectively.[24,25]

$$A + e^- \rightarrow D(\text{CB of PS I}) \quad (3)$$

$$D + h^+ \rightarrow A(\text{VB of PS II}) \quad (4)$$

These are the most common backward reactions occurring in the PS-A/D-PS systems, which lead to the sharp decrease in the effective number of photogenerated electrons and holes. Though some surface treatments, such as Cs-H^+ exchange and deposition of rutile TiO_2, can be used to impede the adsorption of electron acceptor on PS I and donor on PS II, the aforementioned backward reactions cannot still be avoided completely.[26,27] Further, the often used A/D pairs are IO^{3-}/I^-, Fe^{3+}/Fe^{2+}, $[Co(bpy)_3]^{3+/2+}$, $[Co(phen)_3]^{3+/2+}$ and NO_3^-/NO_2^-.[28–31] They all absorb light to the different extent, which decreases the number of adsorbed photons by photocatalysts. Besides, for those A/D pairs it is often difficult to keep the long-term stable state in a wide range of pH, which reduces the number of available A/D pairs. Consequently, the rate of Z-scheme electron transfer between PS II and PS I will be slowed down. Furthermore, due to the chemical nature of the aforementioned A/D pairs, the PS-A/D-PS systems are suitable for the liquid-phase photocatalytic reactions only. Such PS-A/D-PS systems cannot also be used for degradation of pollutants in the solution because the latter can probably hinder the forward redox reaction of the A/D pair. Consequently, the number of the PS-A/D-PS systems is limited in the field of photocatalytic water splitting. Thus, the A/D-free Z-scheme photocatalytic systems attract more and more scientific attention.

As shown in **Figure 5**, an all-solid-state Z-scheme photocatalytic system without A/D pair is constructed by employing conductor (C) as the electron mediator, and can be labeled as PS-C-PS. The insertion of a conductor between PS II and PS I forms the known Ohmic contact with low contact resistance.[32–34] The photogenerated electrons from the CB of PS II can directly

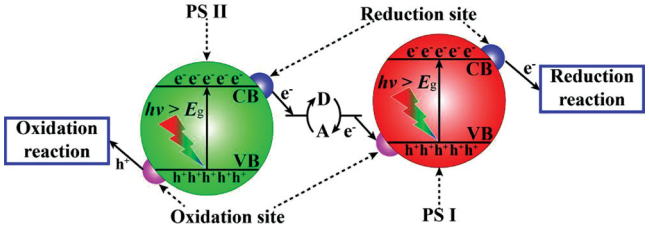

Figure 4. Schematic diagram of Z-scheme electron transfer in PS-A/D-PS system.

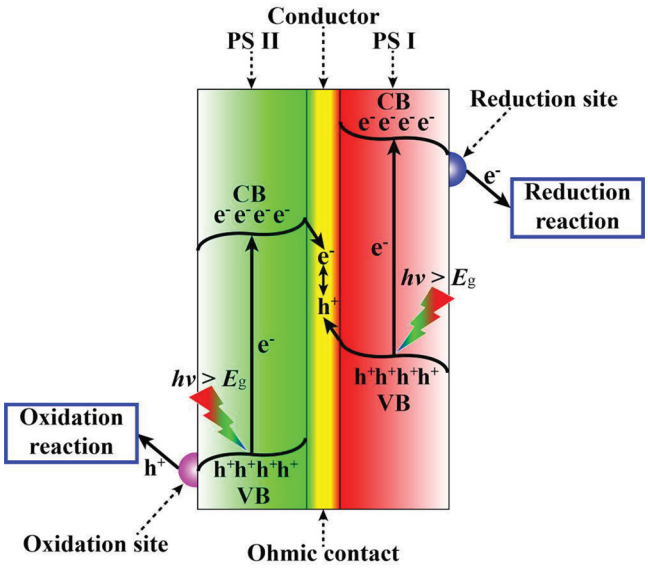

Figure 5. Schematic diagram of Z-scheme electron transfer in a PS-C-PS system.

recombine with the photogenerated holes from the VB of PS I through the Ohmic contact. This reduces the distance of Z-scheme electron transfer. Besides, due to the absence of A/D pair, the aforementioned backward reactions are perfectly avoided. Thus, the photogenerated holes in the VB of PS II and electrons in the CB of PS I can be mostly reserved for the forward oxidation and reduction reactions, respectively. Moreover, the shielding effect of irradiated incident light caused by A/D pair can also be eliminated. Furthermore, without this limitation of A/D pair, the PS-C-PS systems can work in both the gas-phase and liquid-phase environments. Thus, the application range of the PS-C-PS systems is extended from water splitting to solar cells, degradation of pollutants and CO_2 conversion (see **Table 1**).

It is well known that a large number of defects can be easily aggregated at the solid-solid contact interface. Thus, the energy levels of the solid-solid contact interface are quasi-continuous, which is similar to the situation on conductors. This implies that the solid-solid contact interface shows some similar properties to conductors, such as low electric resistance. Therefore, like the conductor in a PS-C-PS system, the solid-solid contact interface can also form the Ohmic contact as shown in **Figure 6**. The constructed Z-scheme photocatalytic system, labeled as PS-PS, is also all-solid-state. In a photocatalytic reaction, the solid-solid contact interface between PS II and PS I serves as the center of photogenerated electron-hole recombination. The two-component PS-PS systems share many properties with the three-component PS-C-PS systems, such as various geometry architectures and wide application range (see **Table 2**). Therefore, the all-solid-state PS-C-PS and PS-PS systems have a larger potential in practical applications than the PS-A/D-PS systems, and attract the most of attention in the future. It is noteworthy that the conductor in the PS-C-PS systems shows generally the stronger ability for charge transfer than in the case of the solid-solid contact interface in the PS-PS systems due to the difference in their electrical resistances. The electrical resistance of the solid-solid contact interface can be tuned by optimizing the formation and treatment of the PS-PS systems.

Though the study of Z-scheme photocatalytic systems is in the initial phase, some successes have been achieved as evidenced by a large number of reports (see reviews[22,69–74] highlighting the significance of these systems). Especially, the all-solid-state Z-scheme systems show many advantages in practical applications. Hence, we believe that a comprehensive review on this topic is desirable for the further development of the Z-scheme photocatalytic systems. This review is mainly focused on the electron mediators, construction, architecture and applications of all-solid-state Z-scheme systems. The key factors influencing their performance are also discussed.

2. PS-C-PS Systems

2.1. Electron Mediators

The Z-scheme TiO_2-Au-CdS system reported in 2006 is the first example of an all-solid-state PS-C-PS system, which is constructed by the photochemical deposition-precipitation method.[35] Firstly, Au nanoparticles (NPs) are deposited on the TiO_2 surface by photoreduction. Secondly, the Au-loaded TiO_2 is dispersed in the ethanol solution containing S_8 molecules. Under ultraviolet light irradiation, Au NPs with large work function can collect the photogenerated electrons from the CB of TiO_2. Thus Au NPs become the reduction sites on the TiO_2 surface. Because of the great affinity of Au surface atoms to sulphur atoms, S8 molecules in ethanol solution are selectively adsorbed on the surface of Au NPs. Next, the collected electrons in Au NPs reduce the adsorbed S_8 molecules into S^{2-}. Meanwhile, Cd^{2+} ions in the solution are bonded to S^{2-} ions on the surface of Au NPs. As a result, the CdS shell is formed around Au NPs (see **Figure 7**). The resulting TiO_2-Au-CdS system exhibits higher photocatalytic activity than the two-component Au-TiO_2 and TiO_2-CdS systems. This is because the presence of Au NPs between TiO_2 and CdS promotes the separation of photogenerated charge carriers in TiO_2 and CdS. It should be noted that the loading of Pt NPs on the CdS shell is still necessary for H_2 production. Besides, the selective photodeposition of Pt NPs on CdS shell further confirms the Z-scheme electron transfer. Moreover, due to the poor visible-light absorption of TiO_2, the C-doped TiO_2 ($TiO_{1.96}C_{0.04}$) was used to replace pure TiO_2, forming the visible-light-response $TiO_{1.96}C_{0.04}$-Au-Pt/CdS system.[36]

In some PS-C-PS systems, the conductor has the same metallic element with PS II or PS I. Under suitable conditions, the conductor can be in-situ generated from photocatalyst. In general, the in-situ formed conductor can be stably embedded on the surface of a photocatalyst, which can inhibit the exfoliation of conductor from the photocatalyst surface as compared to the photodeposition method. Furthermore, the tight solid-solid contact interface between conductor and photocatalyst has low electric resistance, which is beneficial for the formation of Ohmic contact. Silver halides (AgX, X = Cl, Br, I) are famous photosensitive materials with significant application in the photographic field due to their particular photolysis characteristics. Besides, silver halides have also been proved

Table 1. Z-scheme PS-C-PS photocatalytic systems

PS II (available wavelength)	PS I (available wavelength)	Electron mediator	Mass of photocatalyst [g]	Reactant solution	Light source (wavelength/nm)	Application	Activity	QE [%][a]	Ref.
TiO_2 (<387 nm)	Pt/CdS (<540 nm)	Au	0.02	20 mL water	500 W Xe lamp (300 < λ < 400)	H_2 production	10 nmol h^{-1}		[35]
$TiO_{1.96}C_{0.04}$ (<455 nm)	Pt/CdS (<540 nm)	Au	0.15	150 mL Na_2S (0.05 M) + Na_2SO_3 (0.1 M)	Xe arc lamp (>420)	H_2 production	433.2 μmol h^{-1}	23.6 at 420 nm	[36]
AgBr (<490 nm)	AgI (<521 nm)	Ag	0.10	50 mL MO[b] (3.0×10^{-5} M)	500 W Xe lamp (>420)	degradation	DE[c] = 97% (16 h)		[37]
Bi_2WO_6 (<470 nm)	AgBr (<490 nm)	Ag	0.01	50 mL PCP[d] (10 mg L^{-1})	300 W Xe lamp (>420)	degradation	DE = 62% (1 h)		[38]
γ-TaON (<453 nm)	AgCl (<382 nm)	Ag	0.10	100 mL RhB[e] (1×10^{-4} M)	300 W Xe lamp (>420)	degradation	DE = 88% (2 h)		[39]
AgCl (<382 nm)	Graphene oxide (<nm)	Ag	0.03	50 mL MB[f] (2.5×10^{-5} M)	LED lamp (>420)	degradation	DE = 99% (1 h)		[40]
Ag_3PO_4 (<nm)	AgI (<521 nm)	Ag	0.10	100 mL MO (10 mg L^{-1})	500 W Xe lamp (>420)	degradation	DE = 84% (18 min)		[41]
ZnO (<387 nm)	CdS (<540 nm)	Cd	0.10	300 mL Na_2S (0.1 M) + Na_2SO_3 (0.1 M)	300 W Xe lamp (full)	H_2 production	1.17 mmol h^{-1}		[42]
WO_3 (<460 nm)	$PbBi_2Nb_{1.9}Ti_{0.1}O_9$ (<444 nm)	W	0.30	170 mL water + 30 mL CH_3OH	450 W Xe arc lamp (>420)	H_2 production	14.8 μmol h^{-1}	6.06 at 420 nm	[43]
$H_2WO_4{\cdot}H_2O$ (<500 nm)	AgCl (<382 nm)	Ag	0.05	10 mL MO (20 mg L^{-1})	55 W fluorescence lamp (> 420)	degradation	DE = 87% (4 h)		[44]
$Bi_{20}TiO_{32}$ (<534 nm)	AgCl (<382 nm)	Ag	0.10	100 mL RhB (1×10^{-4} M)	300 W Xe lamp (>420)	degradation	DE = 99% (25 min)		[45]
BiOBr (<427 nm)	AgBr (<490 nm)	Ag	0.01	50 mL RhB (10 mg L^{-1})	500 W Xe lamp (>400)	degradation	DE = 99% (44 min)		[46]
WO_3 (<460 nm)	$CaFe_2O_4$ (<670 nm)	ITO[g]	0.10	0.5 L air (CH_3CHO, 500 ppm)	150 W Xe lamp (full)	degradation	DE = 51% (4 h)		[47]
$BiVO_4$ (<520 nm)	Ru/$SrTiO_3$:Rh (<520 nm)	RGO[h]	0.06	120 mL H_2SO_4 (pH 3.5)	300 W Xe lamp (>420)	water splitting	H_2 (11 μmol h^{-1}), O_2 (5.5 μmol h^{-1})	1.03 at 420 nm	[48]
TiO_2 (<387 nm)	CdS (<540 nm)	Au	array (2 cm × 2 cm)	60 mL MB (10 mg L^{-1})	20 W low-pressure mercury lamp (254)	degradation	DE = 72% (2 h)		[49]
TiO_2 (<387 nm)	CdS (<540 nm)	Au	0.05	50 mL Na_2S (0.25 M) + Na_2SO_3 (0.35 M)	750 W Xe-illuminator (full)	H_2 production	3.2 μmol h^{-1}		[50]
ZnO (<387 nm)	CdS (<540 nm)	Au	0.10	270 mL Na_2S (0.1 M) + Na_2SO_3 (0.1 M)	300 W Xe lamp (full)	H_2 production	60.8 μmol h^{-1}		[51]
TiO_2 (<365 nm)	P_2W_{17} (<675 nm)	Pt	0.05 (Pt-TiO_2) + 9.6 mmol P_2W_{17}	8 mL glycerol + 72 mL water	250 W high pressure Hg lamp (>365)	H_2 production	19.6 μmol h^{-1}		[52]
TaON (<500 nm)	RuBLRu′ (<614 nm)	Ag	0.008 (Ag-TaON) + 23 nmol RuBLRu′	4 mL CH_3OH	500-W Hg lamp (>400)	CO_2 reduction	0.1 μmol h^{-1} (HCOOH, CO, H_2)		[53]
Pt/TiO_2 (<387 nm)	InP/[MCE2-A+MCE4] (<918 nm)	Cu	irradiation area (10 mm × 10 mm)	4 mL $NaHCO_3$ (10 mM)	solar simulator (full)	CO_2 reduction	0.22 μmol cm^{-3} h^{-1} (HCOOH)		[54]
Reduced $SrTiO_3$ (<400 nm)	InP/[RuCP] (<900 nm)	Ag	irradiation area (5 mm × 5 mm)	10 ml $NaHCO_3$ (0.1 M)	solar simulator (full)	CO_2 reduction	0.31 μmol h^{-1} (HCOOH)		[55]

[a]Quantum efficiency (QE) = Number of reacted photons ÷ Number of incident photons × 100%;[56] [b]MO: methyl orange; [c]DE (degradation efficiency) = (1 − Equilibrium concentration of pollutant ÷ Initial concentration of pollutant) × 100%; [d]PCP: pentachlorophenol; [e]RhB: rhodamine B; [f]MB: methylene blue; [g]ITO: indium-tin-oxide; [h]RGO: reduced graphene oxide.

to be excellent photocatalysts for the degradation of organic pollutant and inactivation of bacteria. In general, Ag NPs are unavoidably generated in the photocatalytic reaction due to the photo-induced decomposition of AgX. For example, the Z-scheme AgBr-Ag-AgI system was accomplished by irradiating the two-component AgBr-AgI composite with Xe lamp for several seconds.[37] The Ag NPs were in-situ generated in the contact interface between AgBr and AgI. The Z-scheme electron transfer in the AgBr-Ag-AgI system is shown in **Figure 8**. When AgI was substituted for Bi_2WO_6, the Ag NPs can be still in-situ

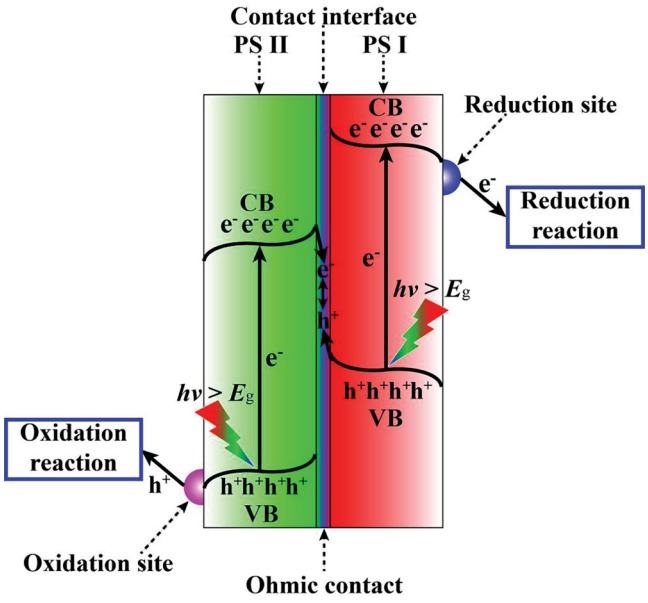

Figure 6. Schematic diagram of Z-scheme electron transfer in PS-PS system.

generated under light irradiation. The resulting Bi_2WO_6-Ag-AgBr system shows the similar Z-scheme electron transfer as the former one.[38] This indicates that Ag and silver halides are suitable for the construction of the Z-scheme PS-C-PS systems. It should be noted that except the in-situ generation of electron mediator from photocatalyst, the photocatalyst can also be in-situ generated from the electron mediator. In the preparation of Z-scheme ZnO-Cd-CdS and WO_3-W-$PbBi_2Nb_{1.9}Ti_{0.1}O_9$ systems, CdS and WO_3 are synthesized by the surface sulfurization of metallic Cd core and the surface oxidation of metallic W cluster, respectively.[42,43] Also, a close solid-solid contact interface can be formed between photocatalyst and conductor.

Many reports show that Ag NPs can respond to the visible light by the surface plasmon resonance (SPR) effect.[75,76] Interestingly, in the Z-scheme AgCl-Ag-$H_2WO_4 \cdot H_2O$ and AgCl-Ag-$Bi_{20}TiO_{32}$ systems, Ag NPs simultaneously serve as the electron mediator and photosensitizer.[44,45] Under the visible-light irradiation ($\lambda > 420$ nm), AgCl with a large E_g of 3.25 eV cannot be photoexcited. However, $H_2WO_4 \cdot H_2O$ and $Bi_{20}TiO_{32}$ can respond to visible light due to their small bandgap (2.48 eV for $H_2WO_4 \cdot H_2O$ and 2.32 eV for $Bi_{20}TiO_{32}$). As shown in **Figure 9**, the photogenerated electrons in the CB of $H_2WO_4 \cdot H_2O$ and $Bi_{20}TiO_{32}$ combine with the photogenerated holes in the highest occupied orbital of Ag. Meanwhile, the photogenerated electrons in the lowest unoccupied orbital of Ag migrate to the CB of AgCl. This is still consistent with the Z-scheme electron transfer discussed before. However, the difference is that the electron mediator assumes the responsibility for the light absorption instead of PS II. This reveals that the band gap of the photocatalyst and wavelength range of incident light synergistically determine the function of Ag NPs in the PS-C-PS system. When both PS II and PS I in the PS-C-PS system can respond to the incident light, the light absorption of Ag NPs is secondary. Thus Ag NPs only act as the electron mediator; but when PS II or PS I cannot absorb the photons from incident light, the light absorption of Ag NPs becomes significant for the Z-scheme photocatalytic reaction. This is further supported by the AgCl-Ag-BiOCl and AgBr-Ag-BiOBr systems.[46] In these two systems, the absorption edges of AgCl, BiOCl, AgBr and BiOBr are 382, 360, 490 and 427 nm, respectively. Therefore, AgCl and BiOCl cannot be photoexcited by visible light ($\lambda >$ 400 nm). The observed photocatalytic activity of the AgCl-Ag-BiOCl system is only attributed to the SPR of Ag NPs (see **Figure 10**a). It should be noted that the produced •Cl is a main active oxidant species in the degradation reaction. However, due to the visible-light responses of AgBr and BiOBr, the Z-scheme electron transfer occurs in the AgBr-Ag-BiOBr systems where Ag NPs only act as the electron mediator (see Figure 10b).

Besides the noble metals discussed above, some low-cost metal oxide and nonmetal materials with excellent conductivity can be also used as the electron mediators in the PS-C-PS systems. In the preparation of WO_3-ITO-$CaFe_2O_4$ system, ITO was firstly coated on the WO_3 surface by the immersion method.[47] Then the mixture of the ITO-modified WO_3 and $CaFe_2O_4$ NPs was calcined at 400 °C. The measurement of acetaldehyde degradation suggests that the ITO coating on the WO_3 surface obviously enhances the visible-light photocatalytic activity as compared to the two-component WO_3-$CaFe_2O_4$ system. Similar to ITO, graphene is also a nonmetallic conductor, which is well known for its outstanding conductivity.[77,78] However, in the practical applications, it is rather difficult to prepare an intact graphene layer due to the generation of numerous defects. Usually, graphene is in the form of the reduced graphene oxide (RGO). In general, the well-reduced graphene oxide GO is believed to favor the improvement of photocatalytic activity. However, the affinity of RGO to photocatalyst also should be considered in the reduction process of GO. For instance, in the Z-scheme $BiVO_4$-RGO-Ru/$SrTiO_3$:Rh system (see **Figure 11**), RGO was obtained by the photocatalytic reduction of GO on the $BiVO_4$ or Ru/$SrTiO_3$:Rh surfaces using methanol as hole scavenger.[48] The formed RGO-$BiVO_4$ (or RGO-Ru/$SrTiO_3$:Rh) was mixed with Ru/$SrTiO_3$:Rh (or $BiVO_4$) in water, respectively. Because the BCB potential of $BiVO_4$ is less negative than that of Ru/$SrTiO_3$:Rh, the RGO on Ru/$SrTiO_3$:Rh surface is reduced to a higher extent than that on the $BiVO_4$ surface. However, the photocatalytic experiments indicate that the $BiVO_4$-RGO-Ru/$SrTiO_3$:Rh system obtained by photoreduction of GO on $BiVO_4$ exhibits higher water-splitting activity than the system prepared by photoreduction of GO on Ru/$SrTiO_3$:Rh. This is due to the hydrophilicity difference between RGO-$BiVO_4$ and RGO-Ru/$SrTiO_3$:Rh. During the photocatalytic reduction of graphene oxide, the elimination of the oxygen-containing groups reduces the hydrophilicity of RGO. As compared to the RGO photoreduced on $BiVO_4$, the RGO photoreduced on Ru/$SrTiO_3$:Rh exhibits higher reduction, higher removal of the oxygen-containing groups and lower hydrophilicity due to the latter having more negative BCB potential. Therefore, it is easy to understand that the dispersion of RGO-Ru/$SrTiO_3$:Rh is more difficult in aqueous solutions, which inhibits the formation of the contact interface between Ru/$SrTiO_3$:Rh and RGO. Consequently, it is not surprising that the photoreduced GO (used as an electron mediator) on Ru/$SrTiO_3$:Rh exhibits lower photocatalytic performance than GO photoreduced on $BiVO_4$.

Table 2. Z-scheme PS-PS photocatalytic systems.

PS II (available wavelength)	PS I (available wavelength)	Mass of photocatalyst (g)	Reactant solution	Light source (wavelength/nm)	Application	Activity	QE (%)	Ref.
$BiVO_4$ (<520 nm)	$Ru/SrTiO_3$:Rh (<540 nm)	0.1 ($BiVO_4$) + 0.2 ($Ru/SrTiO_3$:Rh)	120 mL water (H_2SO_4, pH 3.5)	300 W Xe arc lamp (>420)	water splitting	H_2 (22 μmol h^{-1}), O_2 (9.6 μmol h^{-1})	1.7 at 420 nm	[57]
$Ir/CoO_x/Ta_3N_5$ (<600 nm)	$Ru/SrTiO_3$:Rh (<540 nm)	0.05 ($Ir/CoO_x/Ta_3N_5$) + 0.05 ($Ru/SrTiO_3$:Rh)	250 mL water (H_2SO_4, pH 4.9)	300 W Xe lamp (>420)	water splitting	H_2 (11.4 μmol h^{-1}), O_2 (4.9 μmol h^{-1})		[58]
WO_3 (<460 nm)	$CuBi_2O_4$ (<800 nm)	0.15	CH_3CHO (9000 ppm)	300 W Xe lamp (full)	degradation	DE = 99% (3 h)		[59]
WO_3 (<460 nm)	$NaNbO_3$ (<380 nm)	0.6	300 mL RhB (1 × 10^{-5} M, pH 6.0)	375 W medium pressure mercury lamp (>365)	degradation	DE = 96% (80 min)		[60]
Bi_2O_3 (<nm)	$NaNbO_3$ (<380 nm)	0.6	300 mL RhB (1 × 10^{-5} M, pH 6.0)	375 W medium pressure mercury lamp (>365)	degradation	DE = 97% (80 min)		[61]
WO_3 (<460 nm)	$CaFe_2O_4$ (<670 nm)	0.1	0.5 L air (CH_3CHO, 100 ppm)	150 W Xe lamp (>420)	degradation	DE = 99% (15 h)		[62]
TiO_2 (<387 nm)	g-C_3N_4 (<460 nm)	0.3	15 L air (HCHO, 170 ppm)	15 W UV lamp (365)	degradation	DE = 94% (1 h)		[63]
TiO_2 (<387 nm)	CdS (<540 nm)	irradiation area (1 cm^2), reference electrode (Ag/AgCl)	0.1 M NaOH	300 W Xe lamp (full)	solar cell	photocurrent (0.8 mA), applied potential (0.4 V)		[64]
ZnO (<387 nm)	Pt/CdS (<540 nm)	0.2	300 mL Na_2S (0.1 M) + Na_2SO_3 (0.1 M)	300 W Xe lamp (full)	H_2-production	750 μmol h^{-1}		[65]
Ag/TiN_xO_{2-x} (<800 nm)	$H_3PW_{12}O_{40}$ (<600 nm)	0.01	8 mL MO (5 × 10^{-5} M)	450 W medium pressure Mercury lamp (> 400)	degradation	DE = 99% (35 min)		[66]
IrO_2/TiO_2 (anatase) (<387 nm)	Pt/Si (<1060 nm)	reference electrode (Ag/AgCl)	0.5 M H_2SO_4	300 W Xe lamp (full)	water splitting	H_2 (2.1 μmol h^{-1}), O_2 (1.1 μmol h^{-1})		[67]
$KTaO_3$:Zr (<387 nm)	PtO_x/Cr-TPPCl (< 827 nm)							[68]

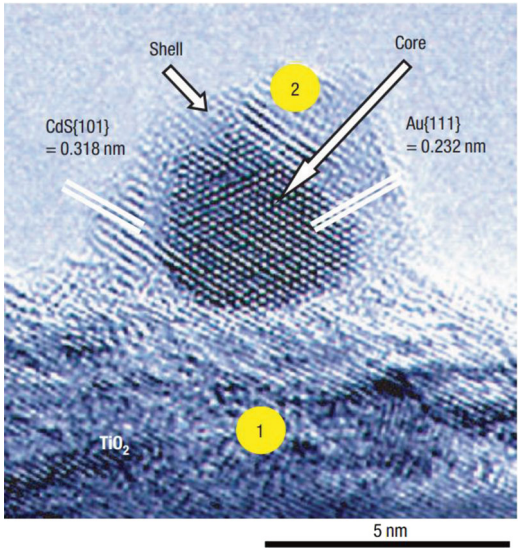

Figure 7. HRTEM image of CdS-Au-TiO_2 nanojunction. Reproduced with permission.[35] Copyright 2006, Nature Publishing Group.

2.2. Geometry Architecture

Geometry architecture of photocatalytic systems is always an important factor that influences their photocatalytic activity. Especially, for the three-component PS-C-PS systems, the architectural design of photocatalytic systems is crucial for light harvesting and charge separation. For example, the one-dimensional nanostructure arrays possess a series of peculiar properties, such as efficient light harvesting, great photoinduced charge separation, remarkable antireflection effect and high specific surface area. In the Z-scheme TiO_2-Au-CdS system, the Au NPs and CdS shells are loaded on the highly ordered TiO_2 hollow nanorod arrays (THNAs) by two-step photodeposition.[49] Thus, many Z-scheme TiO_2-Au-CdS nanojunctions are formed on the surface of TiO_2 hollow nanorods as shown in **Figure 12**. In the photocatalytic reaction, the photogenerated electrons and holes in THNAs and CdS shells can be rapidly separated due to the short distance for charge transfer. This contributes to the high photocatalytic activity of the THNAs-Au-CdS system.

Inspired by antireflection properties of butterfly wings, the wings of *Papilio nephelus* were used as a template to prepare

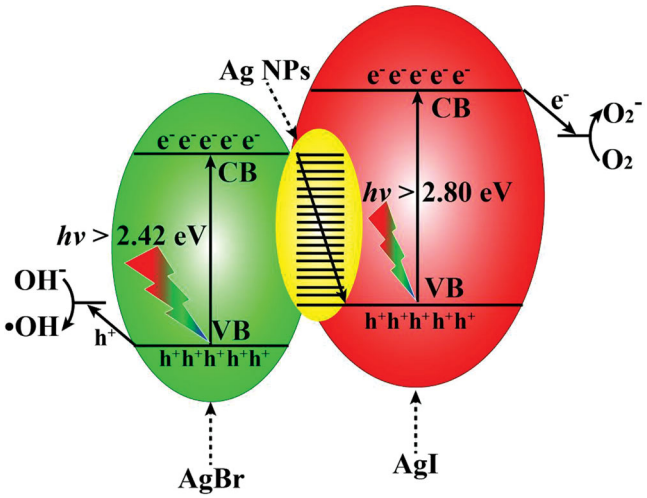

Figure 8. Photocatalytic mechanism of AgI-Ag-AgBr under visible light.

the wing-architecture TiO_2 (WATO) by an immersion-calcination method.[50] WATO consists of the scale-architecture TiO_2 (SATO) and the membrane-architecture TiO_2 (MATO). The Au cores and CdS shells can be loaded on WATO by a similar two-step photodeposition, forming the Z-scheme TiO_2-Au-CdS system (see **Figure 13**). The finite-difference time-domain (FDTD) simulation demonstrates that SATO in WATO has a smaller light reflection and transmission than that in the case of MATO. Besides, SATO has a higher absorbance in water than in air due to the difference in the refraction indices of water and air. However, MATO does not show this type of properties. This is due to the multiple scattering and diffuse reflections of light in the quasi-honeycomb structure of SATO, which prolongs the length of light-transfer path. Moreover, it is suggested that SATO is the main light-harvesting center in the photocatalytic reaction, while the role of MATO is limited

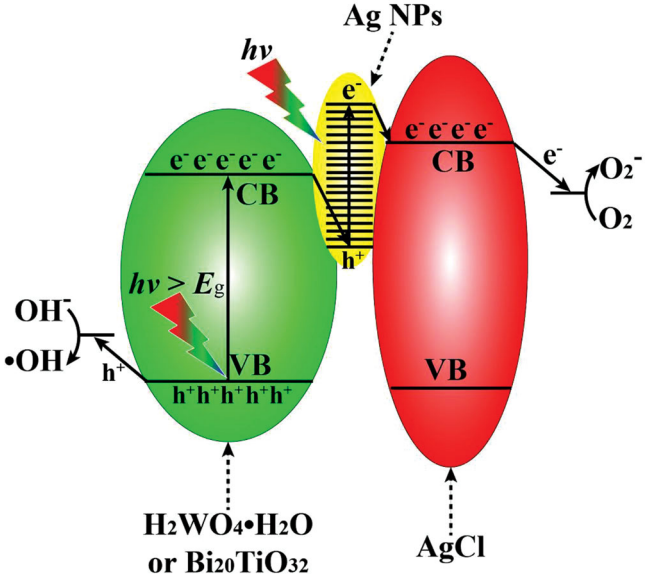

Figure 9. Plasmonic Z-scheme mechanism of the H_2WO_4·H_2O-Ag-AgCl and $Bi_{20}TiO_{32}$-Ag-AgCl systems.

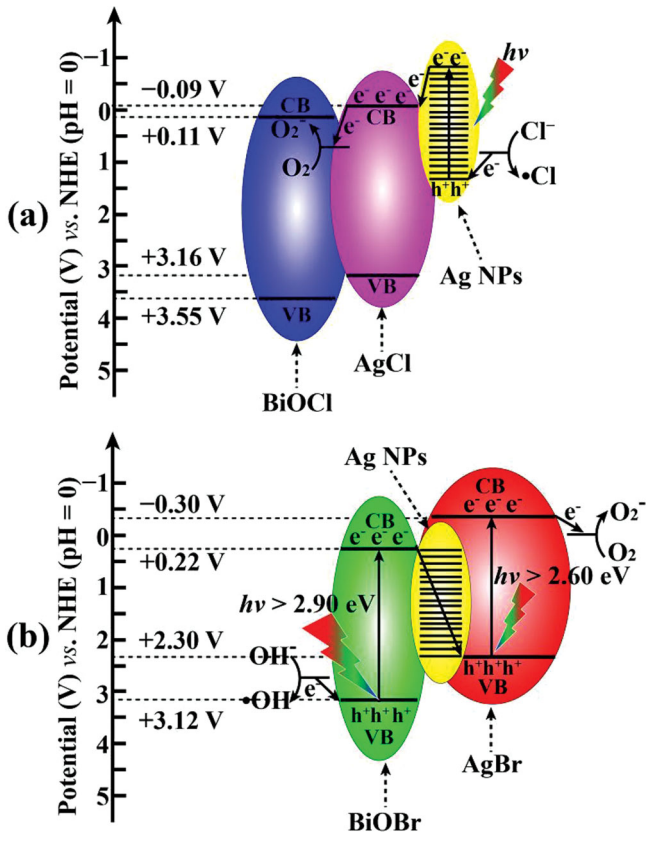

Figure 10. Photocatalytic mechanisms for AgCl-Ag-BiOCl (a) and AgBr-Ag-BiOBr (b).

only to its assistance in light harvesting. As a result, the H_2-production rate of WATO-Au-CdS is about 133% of that of MATO-Au-CdS due to the enhanced light harvesting of SATO. Hence, the bionics is significant for the construction of the PS-C-PS systems.

Based on the crystal structure characteristics of components in the PS-C-PS system, optimizing the geometrical architecture can also improve the photocatalytic efficiency. Along with [001] direction of hexagonal ZnO crystal, the O^{2-}-containing plane and Zn^{2+}-containing plane are stacked in an alternating fashion, resulting in the formations of one O^{2-}-terminated

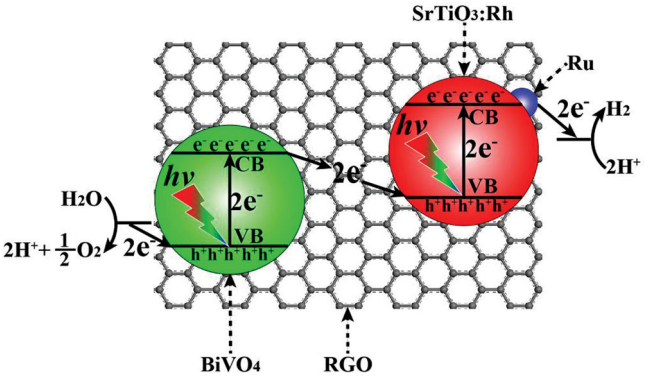

Figure 11. Water-splitting mechanism of $BiVO_4$-RGO-Ru/$SrTiO_3$:Rh.

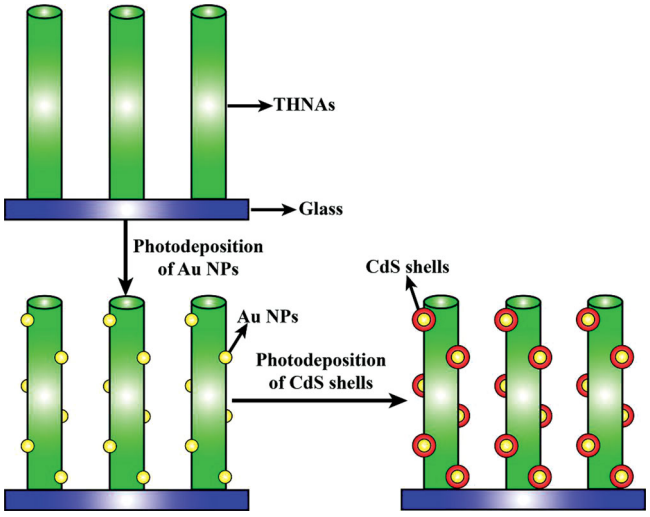

Figure 12. Schematic illustration of the steps involved in the preparation of the THNAs-CdS-Au system.

surface and Zn^{2+}-terminated surface (see **Figure 14**). This pair of surfaces is named polar surfaces, which forms a polarized electric field. The intrinsic polarized electric field of ZnO can promote the separation of photogenerated electrons and holes during photocatalytic reaction. As a result, the photogenerated electrons and holes are accumulated on the Zn^{2+}-terminated and O^{2-}-terminated surfaces, respectively. In the construction of the Z-scheme ZnO-Au-CdS system, the precursor (Au^{3+}) of Au core prefers to be selectively reduced and deposited on the electron-rich Zn^{2+}-terminated {001} surface of hexagonal ZnO nanosheets under ultraviolet-light irradiation (see **Figure 15**a and 15b).[51] Due to the affinity of S^{2-} ions to the Au cores, CdS shells are grown around Au cores by chemical deposition. The formed ZnO-Au-CdS nanojunctions are shown in Figure 15c and 15d. In the Z-scheme photocatalytic reaction, the photogenerated electrons and holes in ZnO are transferred to the Zn^{2+} and O^{2-}-terminated {001} surfaces by the intrinsic polarized electric field, respectively. Then the photogenerated electrons from the CB of ZnO combine with the photogenerated holes from the VB of CdS through Au cores. Finally, the photogenerated electrons in the CB of CdS reduce H^+ into H_2, while the photogenerated holes in the VB of ZnO are consumed by the sacrificial agent from aqueous solution. It is clear

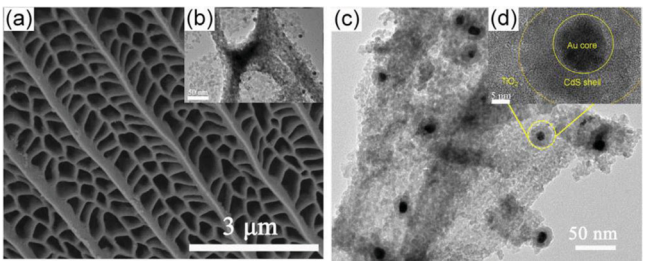

Figure 13. Morphology of Au-WATO, CdS-Au-WATO: (a) FESEM images of Au-WATO; (b) TEM images of Au-WATO; (c) TEM images of CdS-Au-WATO; (d) HRTEM shows CdS-Au with a core-shell structure formed on WATO. Reproduced with permission.[50] Copyright 2013, Elsevier B. V.

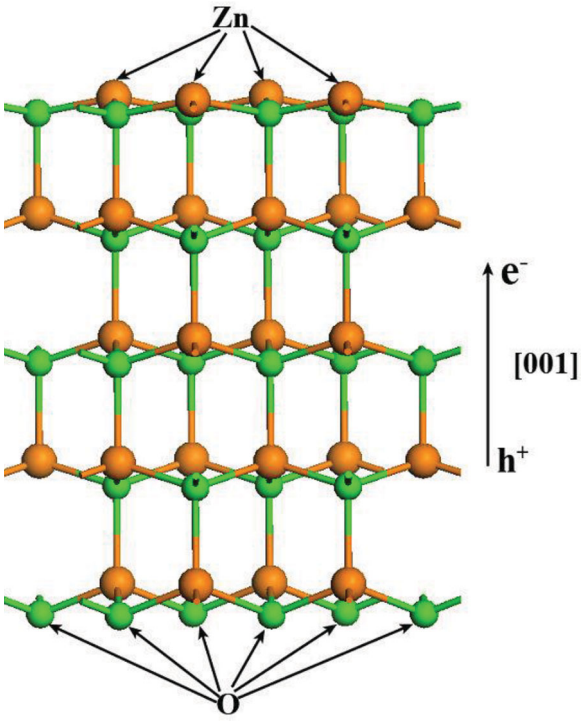

Figure 14. {001} surfaces of hexagonal ZnO. Chocolate and green spheres represent Zn and O atoms, respectively.

that the intrinsic polarized electric field of ZnO not only greatly enhances the rate of Z-scheme electron transfer in ZnO-Au-CdS system, but also effectively restrains the undesirable bulk electron-hole recombination in ZnO. Furthermore, the [001] directions of hexagonal ZnS and CdS and the [111] directions of cubic ZnO, ZnS and CdS possess similar polarized electric fields, which can be also used in the PS-C-PS systems.

Besides the solid-state photocatalysts, some functional groups in the PS-C-PS systems can also perform the function of a photosystem. α_2-$[P_2W_{17}O_{61}]^{10-}$ (P_2W_{17}) with nucleophilic oxo ligands is a typical ion-state photocatalyst for H_2 production.[52] P_2W_{17} can be adsorbed on Pt-loaded TiO_2 surface to form a Z-scheme TiO_2-Pt-P_2W_{17} system. The Pt NPs on the TiO_2 surface collect the photogenerated electrons from the CB of TiO_2 and transfer them to the HOMO of P_2W_{17}. The photogenerated electrons in the LUMO of P_2W_{17} are used to reduce H^+ into H_2, while the photogenerated holes in the VB of TiO_2 are eliminated by sacrificial agent. As compared to P_2W_{17}, the Ru(II) dinuclear supramolecule (RuBLRu′) has a more complex structure, which consist of four parts: $[Ru(dmb)_2(BL)]^{2+}$ (photosensitizer unit), $[Ru(BL)(CO)_2Cl_2]$ (catalyst unit) and two methylphosphonic acid groups (adsorption units) as shown in **Figure 16**a.[53] In combination with the Ag-loaded TaON, RuBLRu′ can reduce CO_2 to HCOOH according to the Z-scheme electron transfer (see Figure 16b). In the photocatalytic reaction, Ag NPs serve as an electron mediator, which collects the photogenerated electrons from TaON. Then, the accumulated electrons in Ag NPs are transferred to the photosensitizer unit of RuBLRu′ and combined with photogenerated holes. Meanwhile, the photogenerated

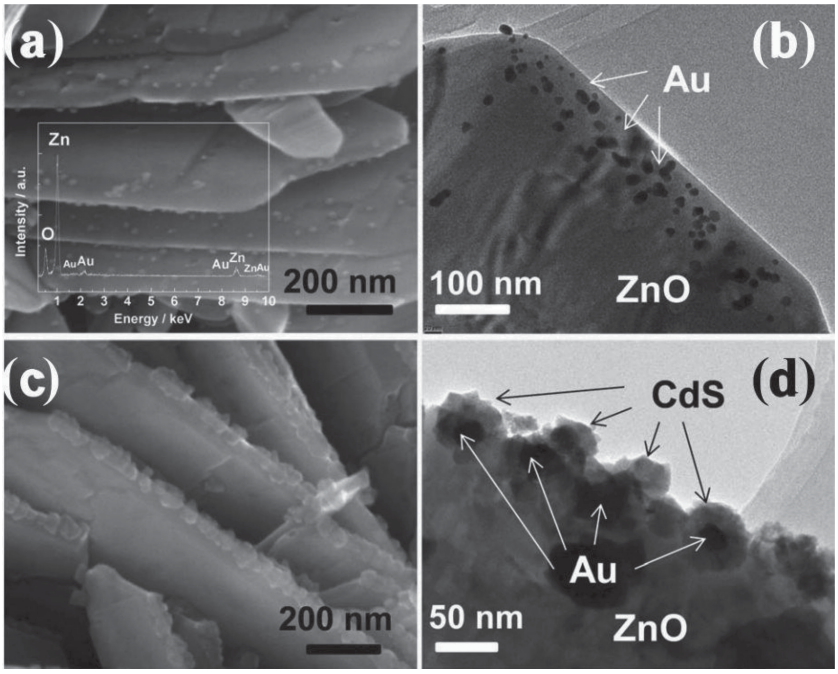

Figure 15. SEM and TEM images of Au-ZnO (a and b); SEM and TEM images of the ZnO-Au-CdS heterostructures (c and d). The inset in (a) is the EDS spectrum of Au-ZnO. Reproduced with permission.[51] Copyright 2013, Royal Society of Chemistry.

electrons in the photosensitizer unit migrate to the catalyst unit and reduce CO_2. The spatial isolation of various functions in RuBLRu′ further enhances the charge separation in the Z-scheme TaON-Ag-RuBLRu′ system. This example shows new opportunities in the design of the multi-function molecular-type photocatalysts.

Similar to the nano-sized PS-C-PS systems above, the photoelectrode-type PS-C-PS systems can also work according to the mechanism of Z-scheme electron transfer. For example, the Pt/TiO_2 photoanode and InP/[MCE2-A+MCE4] (ruthenium complex) photocathode are connected by a copper wire in a two-compartment Pyrex cell separated with a proton exchange membrane, which forms the Z-scheme PS-C-PS system.[54] The photogenerated electrons from the CB of TiO_2 recombine with the photogenerated holes from the VB of InP though the copper wire. Inspired by the aforementioned system, a wireless photoelectrode-type PS-C-PS system was constructed (see **Figure 17**a).[55] The reduced $SrTiO_3$ (r-STO) photoanode and InP/RuCP (ruthenium complex polymer) photocathode were soldered on their backside using Ag paste which functioned as the electron mediator. The Z-scheme photocatalytic reaction was conducted in a one-compartment reactor. The photogenerated electrons from the CB of r-STO recombine with the photogenerated holes from the VB of InP with the assistance of Ag paste (see Figure 17b). A high solar energy conversion efficiency (SECE) of 0.08%, calculated by Equation (5), was achieved for this system.[56]

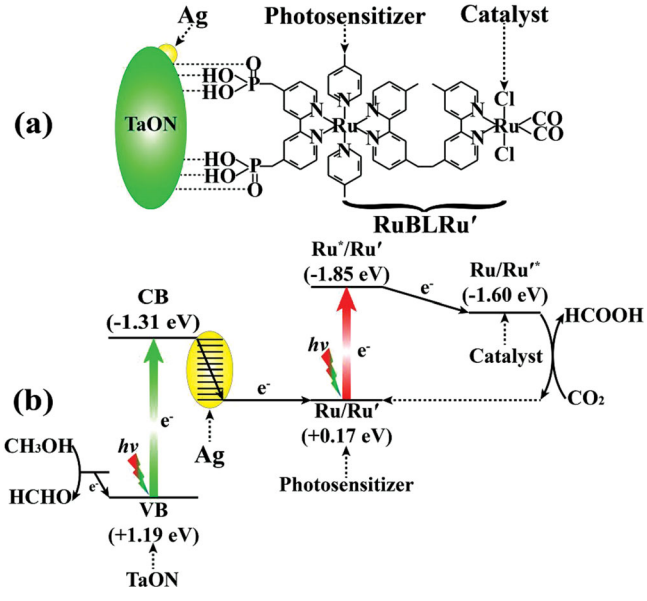

Figure 16. Architecture (a) and Z-Scheme photocatalytic CO_2-reduction mechanism (b) of the TaON-Ag-RuBLRu′ system.

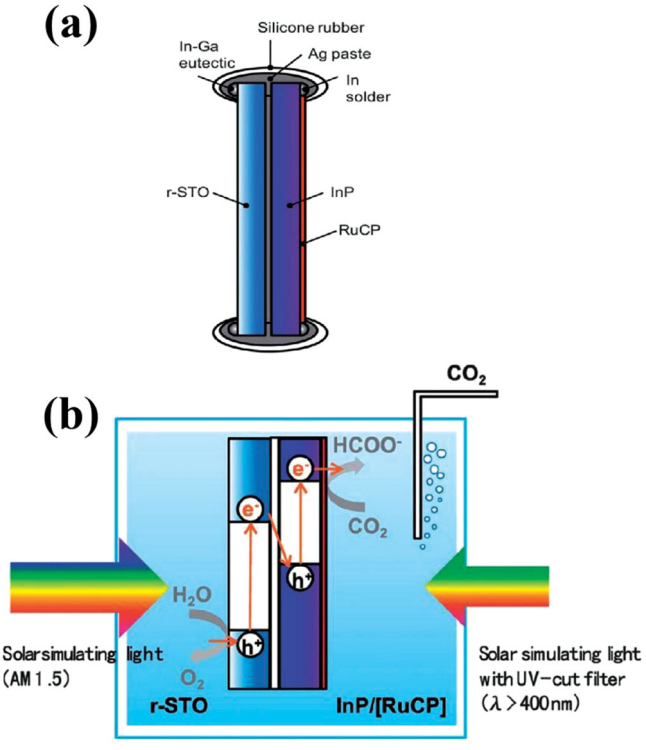

Figure 17. Schematic illustrations of the r-STO-InP/[RuCP] wireless device (a) and one-compartment r-STO-InP/[RuCP] system (b) for the photoelectrochemical reduction of CO_2. Reproduced with permission.[55] Copyright 2013, Royal Society of Chemistry.

$$\text{SECE (\%)} = \text{Output energy of products} \div \text{Energy of incident solar light} \times 100 \quad (5)$$

Due to the limitation of the specific surface area, the number of redox sites available on the photoelectrode is much lower than that provided by nano-sized materials. However, the collection, recycle and transport of photoelectrode-type PS-C-PS systems are convenient.

3. PS-PS Systems

3.1. Formation of the Contact Interface

In the PS-PS systems, the properties of the solid-solid contact interface between PS II and PS I determine the resistance level of electron transfer, which strongly depends on the formation method of the contact interface. Hence, the design of the solid-solid contact interface is important in the construction of Z-scheme PS-PS systems. Based on the properties of the solid-solid contact interface, the formation methods of this interface can be divided into two types: physical and chemical. The physical formation utilizes the interparticle electrostatic adsorption to connect PS II and PS I. When PS II and PS I have opposite charges, the attractive forces are dominant in the PS-PS system, which is beneficial for the formation of the solid-solid contact interface. In contrast, when PS II and PS I have the same charges, the repulsive forces become dominant. This will result in the separation of PS II and PS I, which suppresses the formation of the solid-solid contact interface. It is well known that the type of charge on the solid surface depends on its isoelectric point and pH of the solution. In the Z-scheme $BiVO_4$-Ru/$SrTiO_3$:Rh system constructed by mixing the powders of $BiVO_4$ and Ru/$SrTiO_3$:Rh, the highest photocatalytic activity for water splitting was achieved at pH 3.5.[57] The optical microscope observation revealed that the $BiVO_4$ and Ru/$SrTiO_3$:Rh powders show the most obvious aggregation at pH 3.5 as compared to those at pH 7.0, 4.0 and 2.5 (see **Figure 18**). This is due to the fact that the zeta potential of $BiVO_4$ is negative at pH 2–9 and the isoelectric point of $SrTiO_3$:Rh is about 4. Thus, at pH 3.5, $BiVO_4$ and Ru/$SrTiO_3$:Rh have negative and positive charges, respectively, which is responsible for the electrostatic attraction between $BiVO_4$ and Ru/$SrTiO_3$:Rh powders. The formed solid-solid contact interface contributes to the high QE of 1.7% at 420 nm and the SECE of 0.12%. Similarly, in the Z-scheme Ir/CoO_x/Ta_3N_5-Ru/$SrTiO_3$:Rh system, the highest photocatalytic activity is achieved at pH 3.9 because the isoelectric points of Ta_3N_5 and $SrTiO_3$:Rh are *ca.* 4 and 1, respectively.[58] It can be concluded that the pH value of the reactive solution should be located between the isoelectric points of PS II and PS I, which can promote the formation of solid-solid contact interface. In addition, with a further decrease in pH below 3.9, an appreciable N_2 evolution is observed, implying the self-decomposition of Ta_3N_5. Therefore, the stability of photocatalysts also should be considered in the pH adjustment. Furthermore, exertion of a mechanical force is also an efficient method to form the solid-solid contact interface. For example, the Z-scheme WO_3-$CuBi_2O_4$ system was constructed by extruding WO_3 and $CuBi_2O_4$ powders in a mortar at full hand force; similarly, the Z-scheme WO_3-$NaNbO_3$ system was obtained by ball-milling the mixture of WO_3 and $NaNbO_3$ powders.[59,60]

Different from the physical formation method, the chemical formation method uses one photo-system as a substrate and loads another photo-system onto the surface of the former by chemical reaction. In general, the solid-solid contact interface prepared by chemical formation method is more stable than that obtained by physical formation because the former probably connects PS II and PS I by strong chemical bonds. For example, the Z-scheme TiO_2-C_3N_4 system was constructed by calcination of the mixture of P25 and urea (precursor of C_3N_4). Next, C_3N_4 was directly formed on the surface of P25 particles, resulting in the formation of tight contact interface between C_3N_4 and P25 (see **Figure 19**).[63] Besides the calcination method, the sequential chemical bath deposition is also widely used for the formation of a two-phase contact interface. As a common H_2-production photocatalyst, CdS is easily synthesized by the reaction of Cd^{2+} and S^{2-}. The Z-scheme TiO_2-CdS system can be constructed by successive dipping TiO_2 films into $CdCl_2$ aqueous solution, deionized water, Na_2S aqueous solution and deionized water.[64] The adsorbed Cd^{2+} ions on the surface of TiO_2 film react with S^{2-} ions in the Na_2S aqueous solution to form the CdS NPs. A similar process also occurs in the construction of Z-scheme ZnO-CdS system.[65] Furthermore, for some particular PS-PS systems, containing a molecular-type photosystem, the Z-scheme electron transfer between PS II and PS I depends on the chemical adsorption of the molecular-type photosystem on the surface of the solid-state photosystem. For instance, the Z-scheme Ag/TiN_xO_{2-x}-

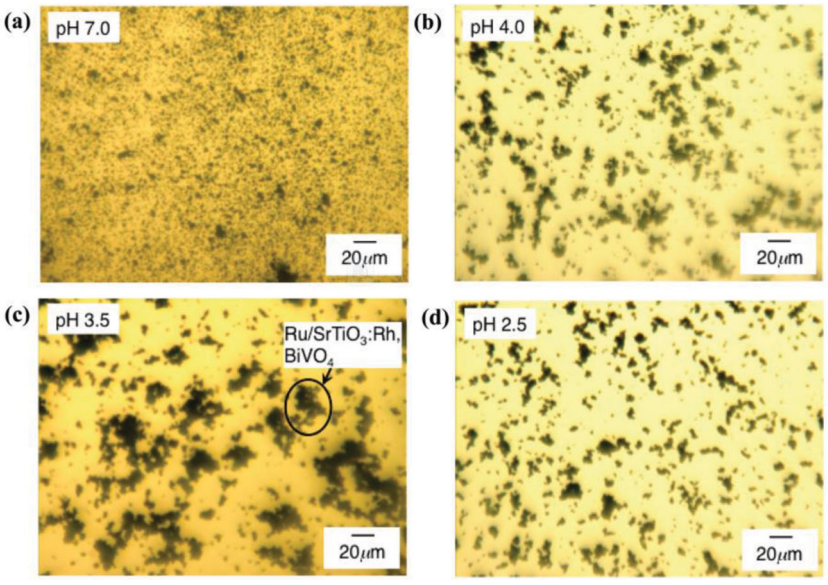

Figure 18. Optical microscope images of pH-adjusted aqueous suspension containing Ru/$SrTiO_3$:Rh and $BiVO_4$ at pH (a) 7.0, (b) 4.0, (c) 3.5, and (d) 3.0. Reproduced with permission.[57] Copyright 2009, American Chemical Society.

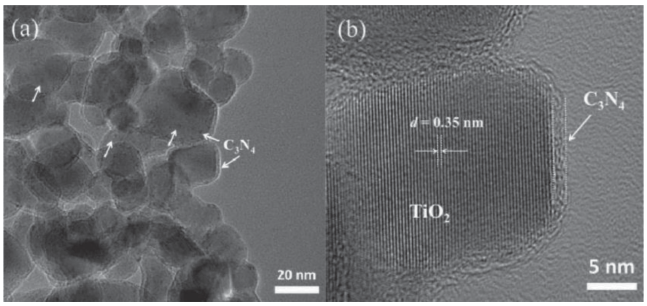

Figure 19. TEM (a) and high-magnification TEM (b) images of g-C_3N_4-TiO_2. Reproduced with permission.[63] Copyright 2013, Royal Society of Chemistry.

$H_3PW_{12}O_{40}$ system was constructed by dispersing the Ag/TiN_xO_{2-x} nanochains in the aqueous solution of $H_3PW_{12}O_{40}$.[66] In the photocatalytic reaction, the photogenerated electrons from the CB of TiN_xO_{2-x} are transferred to the adsorbed $H_3PW_{12}O_{40}$ molecule on the TiN_xO_{2-x} surface through the formed chemical bond between $H_3PW_{12}O_{40}$ molecule and TiN_xO_{2-x}.

In the PS-PS systems, location of the solid-solid contact interface should be also taken into account in the preparation process. A novel Z-scheme TiO_2-Si system was constructed as shown in **Figure 20**a and 20b.[67] In that system, the Si nanowire acted as the trunk, while the TiO_2 nanowires were grown on it as the branches. The solid-solid contact interfaces were formed between the side surface of Si nanowire and the end surface of TiO_2 nanowires. Due to the short carrier-migration distance between Si and TiO_2 nanowires, the photogenerated holes from the VB of Si and the photogenerated electrons from CB of TiO_2 could rapidly recombine at the formed Ohmic contact (see Figure 20c). Thus the tree-shaped Si-TiO_2 system achieved a high SECE (0.12%) under simulated sunlight, which was nearly equal to that of natural photosynthesis. The atomic configuration of the solid-solid contact interface is another factor influencing the Z-scheme electron transfer between PS II and PS I. In the Z-scheme $KTaO_3$:Zr-Pt/Cr-TPPCl (Cr-tetraphenylporphyrin chroride) system, six layers of Cr-TPPCl are adsorbed on the surface of $KTaO_3$:Zr disk (see **Figure 21**).[68] The Cr species in the contact interface serve as the redox centers. In the Z-scheme electron transfer, those redox centers accept the photogenerated electrons from the CB of $KTaO_3$:Zr and transfer them to the HOMO of Cr-TPPCl. It is speculated that the number of redox centers in the solid-solid contact interface determines the rate of Z-scheme electron transfer between PS II and PS I. Hence, the density distribution of redox centers and the area of solid-solid contact interface synergistically determine the rate of Z-scheme electron transfer.

3.2. Optimal Mass Ratio of PS II and PS I

According to the mechanism of the Z-scheme photocatalytic reaction, the photogenerated electrons from the CB of PS II combine with the same quantity of photogenerated holes from the VB of PS I at the solid-solid contact interface. When the number of photogenerated charge carriers in one photo-system is larger than that in another system, the surplus number of

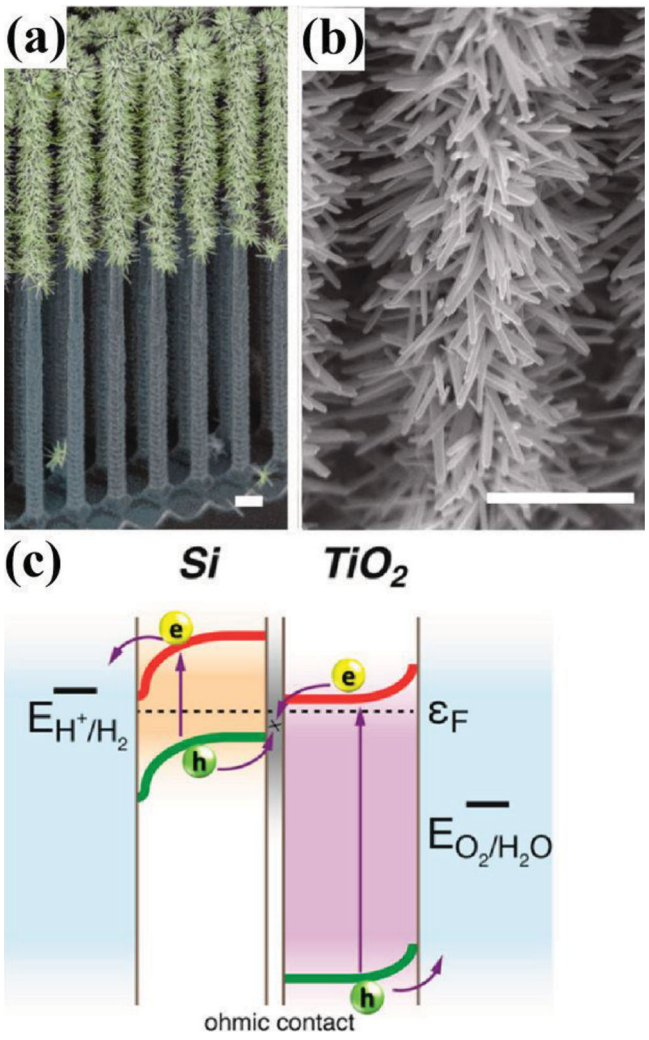

Figure 20. SEM image (a) and magnified SEM image (b) of a tree-shaped TiO_2-Si heterostructure and the corresponding energy band diagram for photocatalytic water splitting (c). Reproduced with permission.[67] Copyright 2013, American Chemical Society.

these charge carriers is probably recombined in the bulk and do not contribute to the Z-scheme photocatalytic reaction. Thus, the ideal situation is that PS II and PS I produce the same number of photogenerated charge carriers. This can be achieved by optimizing the mass (molar) ratio of PS II and PS I. However, the optimal mass (molar) ratio of PS II and PS I is closely related to the geometry architecture of the PS-PS system. For example, the Z-scheme $BiVO_4$-Ru/$SrTiO_3$:Rh system was constructed by simply mixing the $BiVO_4$ and Ru/$SrTiO_3$:Rh powders in the aqueous solution.[57] The highest photocatalytic activity was achieved when the mass ratio of $BiVO_4$ and Ru/$SrTiO_3$:Rh = 1:1. However, the Z-scheme TiO_2-C_3N_4 system showed the highest activity toward formaldehyde degradation when the mass ratio of C_3N_4 and TiO_2 = 3:22.[63] The obvious difference in the optimal mass ratios of $BiVO_4$-Ru/$SrTiO_3$:Rh and TiO_2-C_3N_4 is probably due to their different geometry architectures. In the $BiVO_4$-Ru/$SrTiO_3$:Rh system, the Z-scheme electron transfer depends on the solid-solid contact interface between $BiVO_4$ and Ru/$SrTiO_3$:Rh particles formed by electrostatic interactions

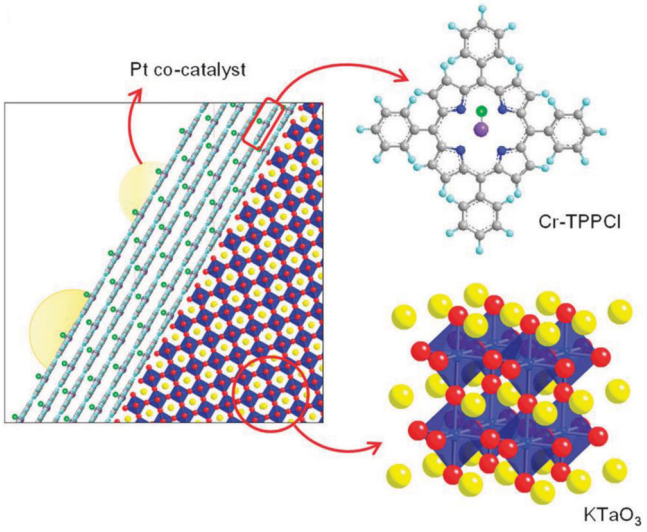

Figure 21. Interface structure of the $KTaO_3$:Zr-Pt/Cr-TPPCl system. Reproduced with permission.[68] Copyright 2011, Royal Society of Chemistry.

(see Figure 18). It should be noted that the solid-solid contact interface between two particles of the same component does not contribute to the Z-scheme electron transfer. Therefore, the excess of any component in the $BiVO_4$-Ru/$SrTiO_3$:Rh system will reduce the effectiveness of the solid-solid contact interface (see **Figure 22**). Besides, the homodispersion of $BiVO_4$ and Ru/$SrTiO_3$:Rh particles is also significant for the formation of effective solid-solid contact interface. However, in the TiO_2-C_3N_4 system, C_3N_4 is chemically deposited on the surface of TiO_2 particles (see Figure 19). When the mass ratio of C_3N_4 and TiO_2 is much lower than 3:22, C_3N_4 is probably sparsely dispersed on the surface of TiO_2 (see **Figure 23**a). The total area of the formed solid-solid contact interface is small, which cannot assure an effective transfer of the photogenerated electrons from TiO_2 to C_3N_4. Therefore, many photogenerated electrons and holes will recombine in C_3N_4 and TiO_2, which reduces the utilization efficiency of solar light. When the mass ratio of C_3N_4 and TiO_2 reaches 3:22, a thin layer of C_3N_4 is formed on the surface of TiO_2 (see Figure 23b). The broaden solid-solid contact interface between C_3N_4 and TiO_2 provides enough channels for the Z-scheme electron transfer. However, the further increase in the mass ratio of C_3N_4 and TiO_2 results in the thicker C_3N_4 layer on the TiO_2 surface (see Figure 23c), which is less effectively penetrated by incident light to reach the TiO_2 surface; consequently, the photoexcitation of TiO_2 is weakened. Thus, the number of photogenerated charge carriers in TiO_2 is much smaller than that in C_3N_4. Besides, the thick C_3N_4 layer extends the distance for the electron transfer from TiO_2 to the C_3N_4 surface, which increases the probability of bulk electron-hole recombination. Moreover, the excessive deposition of C_3N_4 decreases the number of oxidation sites on the TiO_2 surface, which results in inhibiting the generation of •OH for formaldehyde degradation. Similarly, in the TiO_2-CdS and ZnO-CdS systems, CdS is deposited onto the TiO_2 and ZnO surfaces in a chemical bath. The optimal mass percentage of CdS is also much smaller than that of TiO_2 (ZnO).[64,65]

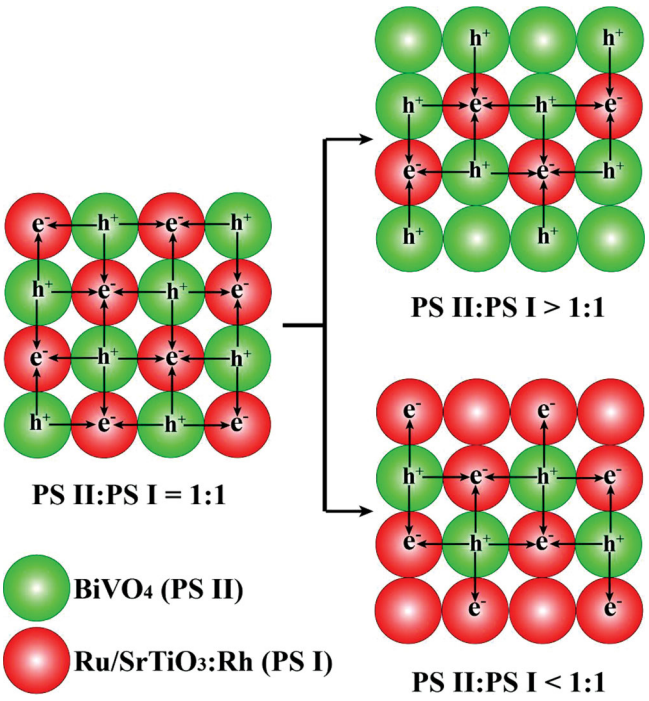

Figure 22. Architectures of the $BiVO_4$-Ru/$SrTiO_3$:Rh system with different mass ratios.

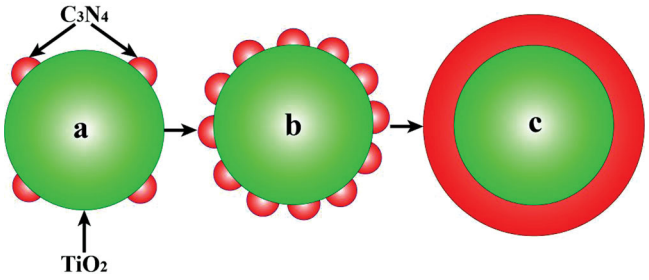

Figure 23. Architectures of the TiO_2-C_3N_4 systems with different mass ratios.

3.3. Verification of Z-Scheme Electron Transfer

Due to the different applications, the PS-PS systems exhibit the diversity in the verification of Z-scheme electron transfer. In the case of the PS-PS systems for water splitting, the verification of Z-scheme electron transfer needs to satisfy three conditions: (a) PS II can only produce O_2 in the presence of electron acceptor, (b) PS I can only produce H_2 in the presence of electron donor, (c) the steady overall water splitting can occur in the simultaneous presence of PS II and PS I and in the absence of electron acceptor and donor. For example, $BiVO_4$ can produce O_2 in the presence of electron acceptor and Ru/$SrTiO_3$:Rh can produce H_2 in the presence of electron donor. When $BiVO_4$ and Ru/$SrTiO_3$:Rh simultaneously exist in the aqueous solution, the stoichiometric amounts of H_2 and O_2 are produced.[57] However, the steady water splitting does not occur in the absence of $BiVO_4$ or Ru/$SrTiO_3$:Rh. This indicates that the photogenerated holes in the VB of $BiVO_4$ and photogenerated electrons in the

CB of $Ru/SrTiO_3$:Rh are used to oxidize and reduce water into O_2 and H_2, respectively. Meanwhile, the photogenerated electrons in the CB of $BiVO_4$ recombine with the photogenerated holes in the VB of $Ru/SrTiO_3$:Rh through the solid-solid contact interface. This is consistent with the Z-scheme electron transfer. Similarly, the Z-scheme electron transfer in CO_2 reduction reaction can also be verified by detecting the oxidation (O_2) and reduction ($C_xH_yO_z$) products.

However, the outlined mechanism is only suitable for the photocatalytic water splitting and CO_2 conversion. For some other Z-scheme photocatalytic reactions such as degradation of pollutants, the aforementioned mechanism is impracticable. The detection of active oxidant species is an indirect method to verify the Z-scheme electron transfer in the photocatalytic degradation. The main active oxidant species include hydroxyl radical (•OH), superoxide anion ($•O_2^-$) and photogenerated hole (h^+), which are produced by the following reactions:

$$OH^- + h^+ \rightarrow •OH, +2.7\ \text{V } \textit{vs.}\ \text{NHE at pH} = 0 \quad (6)$$

$$O_2 + e^- \rightarrow •O_2^-, -0.046\ \text{V } \textit{vs.}\ \text{NHE at pH} = 0 \quad (7)$$

$$h\nu + \text{photocatalyst} \rightarrow h^+ + e^- + \text{photocatalyst},\ h\nu > E_g \quad (8)$$

In general, the roles of •OH, $•O_2^-$ and h^+ in the photocatalytic degradation are determined by comparing the performance of PS-PS system before and after adding their corresponding scavengers. If active oxidant species play a dominant role in the photocatalytic degradation, the addition of its corresponding scavenger will lead to the sharp decrease in the photocatalytic performance of PS-PS system. In contrast, the addition of a scavenger will have a little influence on the photocatalytic performance of PS-PS system if its corresponding active oxidant species play a negligible role in the photocatalytic degradation. The common scavengers for active oxidant species include isopropanol and tert-butanol for •OH, benzoquinone and anthraquinone for $•O_2^-$ and ammonium oxalate and triethanolamine for h^+. In the Z-scheme WO_3-$NaNbO_3$ system for the degradation of rhodamine B (RhB), the TVB potentials (E_{TVB}) of WO_3 and $NaNbO_3$ calculated by Equation (9) are 3.37 and 2.57 V *vs.* NHE at pH = 0, respectively.[60]

$$E_{TVB} = X - E^e + 0.5E_g \quad (9)$$

χ is the absolute electronegativity of the semiconductor, defined as the geometric mean of the absolute electronegativities of the constituent atoms.[79] E^e is the energy of free electrons on the hydrogen scale (*ca.* 4.5 eV). According to Equation (10), the BCB potentials (E_{BCB}) of WO_3 and $NaNbO_3$ are +0.8 and –0.69 V *vs.* NHE at pH = 0, respectively.

$$E_{BCB} = E_{TVB} - E_g \quad (10)$$

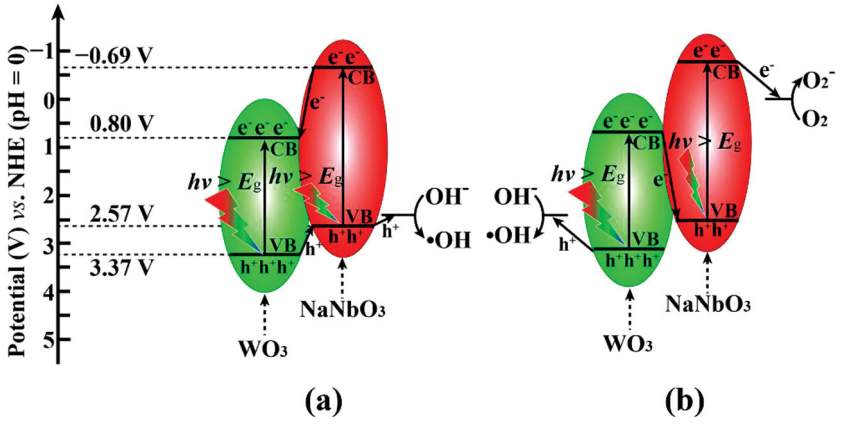

Figure 24. Heterojunction-type (a) and Z-scheme (b) charge-transfer mechanisms for the WO_3-$NaNbO_3$ system.

It was confirmed that the additions of isopropanol, benzoquinone and ammonium all suppressed the photocatalytic activity of WO_3-$NaNbO_3$ system. This suggests that all •OH, $•O_2^-$ and h^+ play significant role in the photocatalytic degradation of RhB. If the photogenerated charge carrier transfer in WO_3 and $NaNbO_3$ occurs via heterojunction-type mechanism (see **Figure 24**a), the photogenarated electrons in the CB of $NaNbO_3$ and the photogenarated holes in the VB of WO_3 will migrate to the CB of WO_3 and the VB of $NaNbO_3$, respectively. As a result, the photogenarated electrons and holes are accumulated in the CB of WO_3 and the VB of $NaNbO_3$, respectively. Due to the positive E_{BCB} (+0.8 V *vs.* NHE at pH = 0) of WO_3, the photogenarated electrons in the CB of WO_3 cannot reduce O_2 into $•O_2^-$ with the redox potential of –0.046 V *vs.* NHE at pH = 0, which is not in agreement with the obtained experimental results. Therefore, the heterojunction-type electron transfer is not dominant in this system. In contrast, according to the Z-scheme electron-transfer path (see Figure 24b), the photogenarated electrons and holes are accumulated in the CB of $NaNbO_3$ and the VB of WO_3, respectively. The E_{BCB} of $NaNbO_3$ (–0.69 V *vs.* NHE at pH = 0) is more negative than the redox potential of $O_2/•O_2^-$. Thus the photogenerated electrons in the CB of $NaNbO_3$ can reduce O_2 into $•O_2^-$. Besides, the E_{TVB} of WO_3 (+3.37 V *vs.* NHE at pH = 0) is more positive than that of $NaNbO_3$ (+2.57 V *vs.* NHE at pH = 0), suggesting that the photogenerated holes in the VB of WO_3 have the stronger oxidizability power than those of $NaNbO_3$. This implies that •OH is easier to be produced by the Z-scheme electron transfer than the heterojunction-type electron transfer. Hence, •OH, $•O_2^-$ and h^+ all play the important role in the photocatalytic degradation of RhB, which well explains the experimental results. The same method can be used to verify the Z-scheme electron transfer in the PS-C-PS systems.

4. Summary and Outlook

A wide absorption range, long-term stability, high charge-separation efficiency and strong redox ability are the key features for any photocatalyst in practical application. However, it is difficult for a single-component photocatalyst to simultaneously possess

all these features. Any artificial multi-component Z-scheme photocatalytic system, simulating the natural photosynthesis process, satisfies the aforementioned requirements. Based on the type of the employed electron mediators, the Z-scheme photocatalytic systems can be divided into three types: PS-A/D-PS, PS-PS and PS-C-PS. They exhibit the obvious differences in the preparation methodology, working mechanism, properties and applications. Especially, the all-solid-state Z-scheme PS-C-PS and PS-PS systems without A/D pair avoid the undesirable backward reactions (3) and (4), which are common in the PS-A/D-PS systems. Besides, the path of Z-scheme electron transfer in the PS-C-PS and PS-PS systems is shortened as compared to that in the PS-A/D-PS systems, which lowers the probability of bulk electron-hole recombination. Moreover, the PS-A/D-PS systems can only work in the liquid-phase environment due to the limitation of A/D pair. However, the PS-C-PS and PS-PS systems can work in the gas-phase and liquid-phase environments. Thus, the PS-C-PS and PS-PS systems have been widely used in the fields of water splitting, solar cells, degradation of pollutants and CO_2 reduction. Hence, the all-solid-state Z-scheme photocatalytic systems have a huge potential for solving the energy and environmental crises facing the industrial development. However, the study of all-solid-state Z-scheme photocatalytic systems is still at an initial stage though numerous efforts have been made so far. The stability, light harvesting, redox ability, charge separation and transportation of the existing all-solid-state Z-scheme photocatalytic systems are far from fulfilling the requirements of practical significance, and need to be further investigated.

For the PS-C-PS systems, the in-situ generation of electron mediator (conductor) can stabilize the semiconductor-metal contact interface, which is beneficial for the formation of Ohmic contact. Except the role of electron mediator, the conductor in the PS-C-PS systems can also act as the photosensitizer due to its SPR effect. However, the dual role of the conductor in the PS-C-PS systems is determined by the wavelength range of incident light and bandgaps of photosystems. By tuning those factors, a high photocatalytic activity can be achieved in the PS-C-PS systems. Geometry architecture of the PS-C-PS systems is another factor influencing its photocatalytic performance because the light harvesting and charge separation strongly depend on the spatial distribution, morphologies and crystal structures of its components. Thus, the optimization of geometry architecture of the PS-C-PS systems creates a great opportunity for further improvement of the photocatalytic performance, which is an important development direction in this area.

As regards the PS-PS systems, the solid-solid contact interface can be built by the physical and chemical methods, which involve the interparticle electrostatic adsorption and heterogeneous nucleation growth, respectively. The former is determined by the isoelectric point of photosystems and pH of the solution, while the latter depends on the preparation process. In the PS-PS systems, the geometry architecture influences the effective area of the solid-solid contact interface and the distribution of incident photons. A broad solid-solid contact interface can promote the recombination of photogenerated electrons from the CB of PS II and holes from the VB of PS I, while the balanced distribution of incident photons between PS II and PS I can maximize the utilization efficiency of solar light. As a result, the optimal mass ratio of PS II and PS I shows obvious architectural diversity in the different PS-PS systems. Besides, the path of Z-scheme electron transfer can be verified by detecting active oxidant species, which is also suitable for the PS-C-PS systems.

It is worth noting that many supramolecular metal complexes have an excellent visible-light absorption, controllable structure and suitable redox potential, which has become the current hot topic. They probably replace the solid-state semiconductor as the photo-system in the next generation of the Z-scheme photocatalytic systems.

Acknowledgements

This work was supported by the 973 program (2013CB632402), and NSFC (51272199, 51320105001, 51372190 and 21177100). Also, this work was financially supported by the Fundamental Research Funds for the Central Universities (2013-VII-030) and Self-determined and Innovative Research Funds of SKLWUT (2013-ZD-1).

Received: January 20, 2014
Revised: March 12, 2014
Published online: May 30, 2014

[1] H. Tong, S. Ouyang, Y. Bi, N. Umezawa, M. Oshikiri, J. Ye, *Adv. Mater.* **2012**, *24*, 229.
[2] M. G. Kibria, H. P. T. Nguyen, K. Cui, S. Zhao, D. Liu, H. Guo, M. L. Trudeau, S. Paradis, A. R. Hakima, Z. Mi, *ACS Nano* **2013**, *7*, 7886.
[3] Q. J. Xiang, J. G. Yu, M. Jaroniec, *J. Am. Chem. Soc.* **2012**, *134*, 6575.
[4] J. A. Christians, R. C. M. Fung, P. V. Kamat, *J. Am. Chem. Soc.* **2014**, *136*, 758.
[5] Q. Zhang, E. Uchaker, S. L. Candelaria, G. Cao, *Chem. Soc. Rev.* **2013**, *42*, 3127.
[6] J. G. Yu, X. X. Yu, *Environ. Sci. Technol.* **2008**, *42*, 4902.
[7] J. Kim, J. Lee, W. Choi, *Chem. Commun.* **2008**, 756.
[8] Y. Bi, S. Ouyang, N. Umezawa, J. Cao, J. Ye, *J. Am. Chem. Soc.* **2011**, *133*, 6490.
[9] E. V. Kondratenko, G. Mul, J. Baltrusaitis, G. O. Larrazábal, J. Pérez-Ramírez, *Energy Environ. Sci.* **2013**, *6*, 3112.
[10] S. C. Roy, O. K. Varghese, M. Paulose, C. A. Grimes, *ACS Nano* **2010**, *4*, 1259.
[11] A. Dhakshinamoorthy, S. Navalon, A. Corma, H. Garcia, *Energy Environ. Sci.* **2012**, *5*, 9217.
[12] J. M. Elward, A. Chakraborty, *J. Chem. Theory Comput.* **2013**, *9*, 4351.
[13] F. L. Formal, S. R. Pendlebury, M. Cornuz, S. D. Tilley, M. Grätzel, J. R. Durrant, *J. Am. Chem. Soc.* **2014**, *136*, 2564.
[14] S. Ida, A. Takashiba, S. Koga, H. Hagiwara, T. Ishihara, *J. Am. Chem. Soc.* **2014**, *136*, 1872.
[15] D. O. Scanlon, C. W. Dunnill, J. Buckeridge, S. A. Shevlin, A. J. Logsdail, S. M. Woodley, C. R. A. Catlow, M. J. Powell, R. G. Palgrave, I. P. Parkin, G. W. Watson, T. W. Keal, P. Sherwood, A. Walsh, A. A. Sokol, *Nat. Mater.* **2013**, *12*, 798.
[16] J. Cao, J. Xing, Y. Zhang, H. Tong, Y. Bi, T. Kako, M. Takeguchi, J. Ye, *Langmuir* **2013**, *29*, 3116.
[17] H. Zheng, Y. Li, H. Liu, X. Yin, Y. Li, *Chem. Soc. Rev.* **2011**, *40*, 4506.
[18] X. H. Li, M. Antonietti, *Chem. Soc. Rev.* **2013**, *42*, 6593.
[19] S. G. Kumar, K. S. R. K. Rao, *Energy Environ. Sci.* **2014**, *7*, 45.
[20] T. Kothe, N. Plumer, A. Badura, M. M. Nowaczyk, D. A. Guschin, M. Rçgner, W. Schuhmann, *Angew. Chem. Int. Ed.* **2013**, *52*, 14233.

[21] A. J. Bard, M. A. Fox, *Acc. Chem. Res.* **1995**, *28*, 141.
[22] K. Maeda, *ACS Catal.* **2013**, *3*, 1486.
[23] R. Abe, K. Sayama, H. Sugihara, *J. Phys. Chem. B* **2005**, *109*, 16052.
[24] K. Sayama, K. Mukasa, R. Abe, Y. Abe, H. Arakawa, *J. Photoch. Photobio. A* **2002**, *148*, 71.
[25] K. Sayama, K. Mukasa, R. Abe, Y. Abe, H. Arakawa, *Chem. Commun.* **2001**, 2416.
[26] Y. Miseki, S. Fujiyoshi, T. Gunji, K. Sayama, *Catal. Sci. Technol.* **2013**, *3*, 1750.
[27] M. Tabata, K. Maeda, M. Higashi, D. Lu, T. Takata, R. Abe, K. Domen, *Langmuir* **2010**, *26*, 9161.
[28] R. Abe, K. Shinmei, N. Koumura, K. Hara, B. Ohtani, *J. Am. Chem. Soc.* **2013**, *135*, 16872.
[29] Y. Sasaki, A. Iwase, H. Kato, A. Kudo, *J. Catal.* **2008**, *259*, 133.
[30] Y. Sasaki, H. Kato, A. Kudo, *J. Am. Chem. Soc.* **2013**, *135*, 5441.
[31] K. Sayama, R. Abe, H. Arakawa, H. Sugihara, *Catal. Commun.* **2006**, *7*, 96.
[32] Saji Thomas Kochuveedu, Yoon Hee Jang, Dong Ha Kim, *Chem. Soc. Rev.* **2013**, *42*, 8467.
[33] K. E. Byun, H. J. Chung, J. Lee, H. Yang, H. J. Song, J. Heo, D. H. Seo, S. Park, S. W. Hwang, I. Yoo, K. Kim, *Nano Lett.* **2013**, *13*, 4001.
[34] F. Ou, D. B. Buchholz, F. Yi, B. Liu, C. Hseih, R. P. H. Chang, S. T. Ho, *ACS Appl. Mater. Inter.* **2011**, *3*, 1341.
[35] H. Tada, T. Mitsui, T. Kiyonaga, T. Akita, K. Tanaka, *Nat. Mater.* **2006**, *5*, 782.
[36] H. J. Yun, H. Lee, N. D. Kim, D. M. Lee, S. Yu, J. Yi, *ACS Nano* **2011**, *5*, 4084.
[37] H. Lin, J. Cao, B. Luo, B. Xu, S. Chen, *Catal. Commun.* **2012**, *21*, 91.
[38] L. Zhang, K. H. Wong, Z. Chen, J. C. Yu, J. Zhao, C. Hu, C. Y. Chan, P. K. Wong, *Appl. Catal. A* **2009**, *363*, 221.
[39] J. Hou, C. Yang, Z. Wang, Q. Ji, Y. Li, G. Huang, S. Jiao, H. Zhu, *Appl. Catal. B* **2013**, *142–143*, 579.
[40] Y. Min, G. He, Q. Xu, Y. Chen, *J. Mater. Chem. A* **2014**, *2*, 1294.
[41] Z. Chen, W. Wang, Z. Zhang, X. Fang, *J. Phys. Chem. C* **2013**, *117*, 19346.
[42] X. Wang, G. Liu, L. Wang, Z. Chen, G. Q. Lu, H. M. Cheng, *Adv. Energy Mater.* **2012**, *2*, 42.
[43] H. G. Kim, E. D. Jeong, P. H. Borse, S. Jeon, K. Yong, J. S. Lee, W. Li, S. H. Oh, *Appl. Phys. Lett.* **2006**, *89*, 64103.
[44] X. Wang, S. Li, Y. Ma, H. Yu, J. G. Yu, *J. Phys. Chem. C* **2011**, *115*, 14648.
[45] J. Hou, Z. Wang, C. Yang, W. Zhou, S. Jiao, H. Zhu, *J. Phys. Chem. C* **2013**, *117*, 5132.
[46] L. Ye, J. Liu, C. Gong, L. Tian, T. Peng, L. Zan, *ACS Catal.* **2012**, *2*, 1677.
[47] Z. Liu, Z. G. Zhao, M. Miyauchi, *J. Phys. Chem. C* **2009**, *113*, 17132.
[48] A. Iwase, Y. H. Ng, Y. Ishiguro, A. Kudo, R. Amal, *J. Am. Chem. Soc.* **2011**, *133*, 11054.
[49] H. Zhu, B. Yang, J. Xu, Z. Fu, M. Wen, T. Guo, S. Fu, J. Zuo, S. Zhang, *Appl. Catal. B* **2009**, *90*, 463.
[50] L. Ding, H. Zhou, S. Lou, J. Ding, D. Zhang, H. Zhu, T. Fan, *Int. J. Hydrogen Energ.* **2013**, *38*, 8244.
[51] Z. B. Yu, Y. P. Xie, G. Liu, G. Q. Lu, X. L. Ma, H. M. Cheng, *J. Mater. Chem. A* **2013**, *1*, 2773.
[52] N. Fu, Z. Jin, Y. Wu, G. Lu, D. Li, *J. Phys. Chem. C* **2011**, *115*, 8586.
[53] K. Sekizawa, K. Maeda, K. Domen, K. Koike, O. Ishitani, *J. Am. Chem. Soc.* **2013**, *135*, 4596.
[54] S. Sato, T. Arai, T. Morikawa, K. Uemura, T. M. Suzuki, H. Tanaka, T. Kajino, *J. Am. Chem. Soc.* **2011**, *133*, 15240.
[55] T. Arai, S. Sato, T. Kajino, T. Morikawa, *Energy Environ. Sci.* **2013**, *6*, 1274.
[56] Z. Chen, T. F. Jaramillo, T. G. Deutsch, A. K. Shwarsctein, A. J. Forman, N. Gaillard, R. Garland, K. Takanabe, C. Heske, M. Sunkara, E. W. McFarland, K. Domen, E. L. Miller, J. A. Turner, H. N. Dinh, *J. Mater. Res.* **2010**, *25*, 3.
[57] Y. Sasaki, H. Nemoto, K. Saito, A. Kudo, *J. Phys. Chem. C* **2009**, *113*, 17536.
[58] S. S. K. Ma, K. Maeda, T. Hisatomi, M. Tabata, A. Kudo, K. Domen, *Chem. Eur. J.* **2013**, *19*, 7480.
[59] T. Arai, M. Yanagida, Y. Konishi, Y. Iwasaki, H. Sugihara, K. Sayama, *J. Phys. Chem. C* **2007**, *111*, 7574.
[60] S. Chen, L. Ji, W. Tang, X. Fu, *Dalton Trans.* **2013**, *42*, 10759.
[61] S. Chen, Y. Hu, L. Ji, X. Jiang, X. Fu, *Appl. Surf. Sci.* **2014**, *292*, 357.
[62] M. Miyauchi, Y. Nukui, D. Atarashi, E. Sakai, *ACS Appl. Mater. Inter.* **2013**, *5*, 9770.
[63] J. G. Yu, S. H. Wang, J. X. Low, W. Xiao, *Phys. Chem. Chem. Phys.* **2013**, *15*, 16883.
[64] X. W. Wang, G. Liu, L. Z. Wang, J. Pan, G. Q. Lu, H. M. Cheng, *J. Mater. Chem.* **2011**, *21*, 869.
[65] X. W. Wang, G. Liu, Z. G. Chen, F. Li, L. Z. Wang, G. Q. Lu, H. M. Cheng, *Chem. Commun.* **2009**, 3452.
[66] H. Lee, J. Lee, Y, H. Lee , J. Lee, M. Yoon, *J. Mater. Chem.* **2011**, *21*, 12829.
[67] C. Liu, J. Tang, H. M. Chen, B. Liu, P. Yang, *Nano Lett.* **2013**, *13*, 2989.
[68] H. Hagiwara, T. Inoue, S. Ida, T. Ishihara, *Phys. Chem. Chem. Phys.* **2011**, *13*, 18031.
[69] Y. Q. Qu, X. F. Duan, *Chem. Soc. Rev.* **2013**, *42*, 2568.
[70] R. M. Navarro, M. C. Alvarez-Galvan, J. A. V. Mano, S. M. Al-Zahrani, J. L. G. Fierro, *Energy Environ. Sci.* **2010**, *3*, 1865.
[71] A. Kudo, Y. Miseki, *Chem. Soc. Rev.* **2009**, *38*, 253.
[72] M. Kitano, M. Hara, *J. Mater. Chem.* **2010**, *20*, 627.
[73] W. Fan, Q. Zhang, Y. Wang, *Phys. Chem. Chem. Phys.* **2013**, *15*, 2632.
[74] G. Liu, L. Wang, H. G. Yang, H. M. Cheng, G. Q. Lu, *J. Mater. Chem.* **2010**, *20*, 831.
[75] M. R. Jones, K. D. Osberg, R. J. Macfarlane, M. R. Langille, C. A. Mirkin, *Chem. Rev.* **2011**, *111*, 3736.
[76] W. Hou, S. B. Cronin, *Adv. Funct. Mater.* **2013**, *23*, 1612.
[77] Q. J. Xiang, J. G. Yu, M. Jaroniec, *Chem. Soc. Rev.* **2012**, *41*, 782.
[78] G. Xie, K. Zhang, B. Guo, Q. Liu, L. Fang, J. R. Gong, *Adv. Mater.* **2013**, *25*, 3820.
[79] Y. Xu, M. A. A. Schoonen, *Am. Mineral.* **2000**, *85*, 543.